

# Measurement of X-ray photons using an INGRID chip

Master-Arbeit  
zur Erlangung des akademischen Grades  
Master of Science  
(M.SC.)  
der Universität Siegen



Department Physik

vorgelegt von  
Jan Joachim Hahn

August 2020



# Contents

<b>Acronyms</b>	<b>iii</b>
<b>1 Introduction</b>	<b>1</b>
1.1 The standard model of particle physics . . . . .	1
1.2 Axions and axion like particles (ALPs) . . . . .	5
1.3 Detection of axions and ALPs . . . . .	11
<b>2 Theoretical background of gaseous detectors</b>	<b>19</b>
2.1 Generation of charge carriers . . . . .	19
2.2 Behaviour of free charge carriers in gas . . . . .	22
2.3 Readout of drift chambers . . . . .	24
<b>3 Experimental setup</b>	<b>29</b>
3.1 Gas supply . . . . .	29
3.2 International Axion Observatory (IAXO) test chamber . . . . .	31
3.3 Signal generation . . . . .	33
3.4 Readout . . . . .	35
3.5 Expected behaviour . . . . .	35
<b>4 Data handling and analysis</b>	<b>39</b>
4.1 General concept of reconstruction . . . . .	39
4.2 Reader . . . . .	40
4.3 Analysis package . . . . .	40
<b>5 Measurements and results</b>	<b>47</b>
5.1 Commissioning stage . . . . .	47

5.2	First test using Fe-55 . . . . .	48
5.3	Results for different X-ray sources . . . . .	57
5.4	Additional analysis . . . . .	63
<b>6</b>	<b>Conclusion</b>	<b>71</b>
	<b>Bibliography</b>	<b>73</b>

## Acronyms

<b>ALP</b>	axion like particle
<b>ASIC</b>	application-specific integrated circuit
<b>ATLAS</b>	A Toroidal LHC ApparatuS
<b>CAST</b>	CERN axion solar telescope
<b>CCD</b>	charge-coupled device
<b>CKM</b>	Cabibbo–Kobayashi–Maskawa
<b>CMOS</b>	complementary metal–oxide–semiconductor
<b>CMS</b>	Compact Muon Solenoid
<b>CSA</b>	charge sensitive amplifier
<b>CTA</b>	Cherenkov Telescope Array
<b>eV</b>	electron volt
<b>FOM</b>	figure of merit
<b>GEM</b>	gas electron multiplier
<b>HDMI</b>	high definition multimedia interface
<b>IAXO</b>	International Axion Observatory
<b>LASER</b>	light amplification by stimulated emission of radiation
<b>LHC</b>	Large Hadron Collider
<b>MCA</b>	multi channel analyzer
<b>MICOMEGAS</b>	Micro-MESh Gaseous Structure
<b>MIP</b>	minimal ionising particle
<b>MPGD</b>	micropattern gas detector
<b>MST</b>	medium-sized telescope
<b>MWPC</b>	multi-wire proportional chamber
<b>PCB</b>	printed circuit board
<b>PMNS</b>	Pontecorvo-Maki–Nakagawa–Sakata
<b>PQ</b>	Peccei Quinn

<b>PVC</b>	polyvinylchloride
<b>QCD</b>	quantum chromodynamics
<b>QED</b>	quantum electrodynamics
<b>QFT</b>	quantum field theory
<b>RMS</b>	root mean square
<b>ROI</b>	region of interest
<b>SDD</b>	silicon drift detector
<b>SHV</b>	safe high voltage
<b>SM</b>	standard model of particle physics
<b>TES</b>	Transition Edge Sensor
<b>TOA</b>	time of arrival
<b>TOS</b>	Timepix Operating Software
<b>TOT</b>	time over threshold
<b>TPC</b>	time projection chamber
<b>TTL</b>	transistor-transistor logic
<b>UV</b>	ultra violet
<b>vev</b>	vacuum expectation value

This chapter will first give a short introduction to the standard model of particle physics (SM), its particles and interactions. The next part will show the motivation for the introduction of new particles, axions, in the SM and give a short overview of different models and their phenomenology. This will be followed by a description of helioscopes for detection of axions produced in the sun, including the components and performance of different current and future helioscopes. The usual convention of  $\hbar = c = 1$  is used in this chapter and the rest mass of particles is just referred to as mass. The electrical charge of particles is referred to as charge.

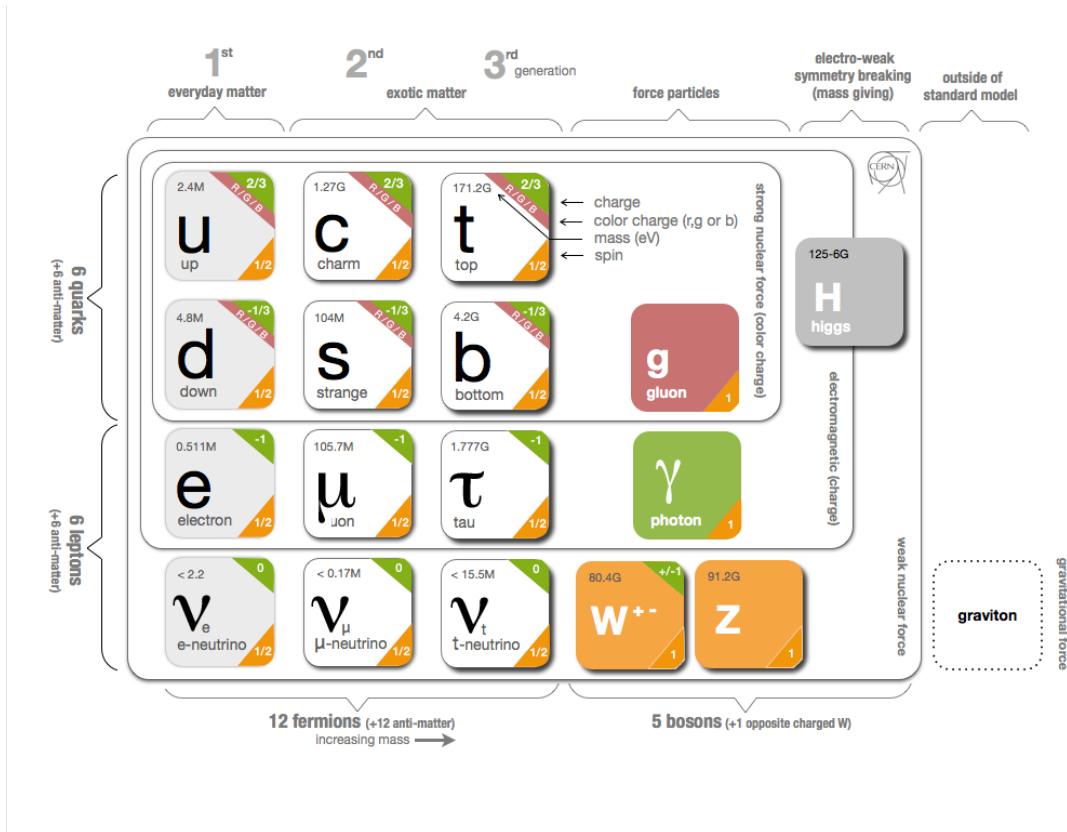
## 1.1 The standard model of particle physics

The SM is currently the best model to describe elementary particles and their interactions. It is a quantum field theory (QFT) and has three forces and twelve elementary particles. For each particle exists an anti-particle with same mass and opposite charges. The forces are electromagnetic, described by quantum electrodynamics (QED), strong interaction, described by quantum chromodynamics (QCD), and weak interaction. Weak and electromagnetic interactions can be unified to the electroweak interaction. The force carriers are called gauge bosons and they are described in more detail in part 1.1.2. To introduce the particle masses, the Higgs-mechanism introduces an additional particle, the Higgs boson.

### 1.1.1 Particles in the SM

The twelve elementary particles of the SM are fermions with spin  $\frac{1}{2}$ . All of them interact via the weak interactions, while only those that carry electrical charge participate in the electromagnetic interactions. This excludes the neutrinos from the QED, while both, quarks and charged leptons, participate. For the strong interaction, the particles have to carry

colour charge, meaning only quarks participate in the QCD. The particles are sorted in three generations of increasing mass, but only the first generation quarks and charged leptons, as well as all neutrinos, are stable and do not decay. These are up quark, down quark, electron and neutrinos. In table 1.1 the different particles and interactions are shown, including their masses. It should be noted that for each particle, there is a corresponding anti-particle with identical mass and spin, but opposite sign for all types of charge and flavour.



Tab. 1.1: Particles of the SM. The different particles with exception of the graviton are described in the text [Pur12].

### Leptons

The six leptons of the SM are grouped in three pairs called generations, each consisting of a charged lepton and a uncharged lepton neutrino. The charged lepton masses increase with the generation, while the neutrino masses are very small. Each lepton generation carries an additional property called flavour, associated with a quantum number called lepton family number. For example an electron or electron neutrino carry one count of electron flavour and zero counts of muon or tau flavour. The sum of the three flavours is the lepton



number, and both lepton family number and lepton number are conserved in interactions. Lepton universality is the property that all interactions of leptons are independent of the flavour, except for kinematic differences because of the different masses. The current limit on the mass of neutrinos is  $m_{\nu_e} < 1\text{eV}$  (90% CL) [Ake+19], compared to the electron mass  $m_e = 511\text{keV}$ . Neutrino oscillation experiments indicate different masses for the neutrinos, but are only capable of observing the squared differences between the neutrino masses. These mass splittings suggest very small neutrino masses for all flavours. Mixing between the different generations of leptons only happens for the neutrinos in the form of neutrino mixing by the Pontecorvo-Maki-Nakagawa-Sakata (PMNS) matrix, while in the interactions the lepton number and lepton family number is conserved. This also indicates that neutrinos observed in interactions are eigenstates of the interaction, but these eigenstates are not the mass eigenstates. In many cases, the assumption of massless neutrinos is valid.

## Quarks

The six quarks are grouped in three pairs. Depending on their electrical charge, they are called up-type for  $\frac{2}{3}e$  charge and down-type for  $-\frac{1}{3}e$  charge. All quarks carry one of the three colour charges of QCD, while anti-quarks carry anti-colour. They also carry flavour, which is conserved in all interactions except in weak interactions mediated by the W-boson. By convention, all quarks of the second and third generation carry a flavour. The flavour of the first generation quarks is usually not specified, because charge and lack of other flavours are sufficient to identify the flavour. The second generation quarks are the ones with strangeness or charm, while the flavours of the third generation are topness and bottomness. For example, the strange quark carries a strangeness of 1, while all other flavours are zero and the charge is  $-\frac{1}{3}e$ . A important phenomenon of quarks is confinement, an effect of the strong interaction. Confinement prevents the detection of single quarks by forcing quarks to combine to colourless mesons of integer spin (quark and anti-quarks) or baryons of half-integer spin (three quarks).

### 1.1.2 The gauge bosons

The gauge bosons are the force carriers of the interactions and all of them are of spin 1. There is the photon, two W bosons, one Z boson and eight gluons.

#### Photon

For the electromagnetic interaction, the gauge boson is the massless photon. It couples to electric charge and carries no charge itself (neither colour nor electric). Thus there is no photon photon vertex in the SM and interactions between photons are only possible

by higher order processes like Delbrück scattering, with a fermion loop coupling to both photons.

### W and Z boson

The weak interaction has three massive force carriers. There are the two charged W bosons,  $W^+$  and  $W^-$ , with a mass of 80 GeV, as well as the neutral Z boson with a mass of 91 GeV. The W bosons couple between charged and uncharged leptons within the same generation, as well as between all combinations of one up-type and one down-type quark. The coupling strength between different quark flavours is modified by the Cabibbo–Kobayashi–Maskawa (CKM) matrix, suppressing couplings between the generations. More precisely, the eigenstates for the weak interaction are not the mass eigenstates and the CKM matrix describes the decomposition of mass into weak eigenstates, very similar to the PMNS matrix for the neutrinos. The Z boson in contrast couples to any two fermions, as long as all conservation laws are not violated. In contrast to electromagnetic interaction, direct couplings between W and Z bosons exist. The high mass of the gauge bosons suppresses the weak interaction at low energies and so far CP violation has only been observed in weak interactions.

### Gluons

In the case of the strong interaction, eight massless gluons are the gauge bosons, without electric charge but carrying the colour charge of strong interaction. Thus they couple only to quarks and other gluons. They always carry colour charge and anti-colour charge and form an octet. In an interaction with gluons the colour of a quark always changes.

#### 1.1.3 The Higgs boson

The mass terms of the W and Z bosons causes problems for the gauge freedom of the SM. A solution of this is the Higgs mechanism. It works by introducing a new potential with couplings to all massive particles. This new field is the Higgs field and its potential of the form  $V(\Phi) = a|\Phi|^4 + |\Phi|^2$  is often referred to as Mexican hat or Higgs potential. The minima of the potential are not at zero field strength. The position of the minimum is the vacuum expectation value (vev) of the field. The expansion around the vev leads to several terms in the Lagrangian, which contain a coupling to the excitations of the Higgs field, leading to Higgs couplings, and to the vev. These couplings to the vev are the desired mass terms. A self interaction of the Higgs leads to Higgs-Higgs interactions and the coupling to the vev gives rise to a massive Higgs. The Higgs boson was discovered at the Large Hadron Collider (LHC) by both A Toroidal LHC ApparatuS (ATLAS) and Compact Muon Solenoid (CMS) in 2012 at a mass of 125 GeV [Aad+12]. Different masses of particles are reflected

by a different coupling strength, since their masses are proportional to the product of vev and coupling strength. This influences also the coupling of the Higgs boson, coupling more strongly to heavy particles.

## 1.2 Axions and ALPs

Axions and ALPs appear in different models. For an overview, refer for example to [Tan+18], chapter 111 or [Arm+19]. The following section will contain some of the reasons for the introduction of a new symmetry leading to axions, a short description of the original model, as well as two more recent models.

### 1.2.1 The strong CP problem

As a non-abelian gauge theory, the strong interaction may have several ground states and transitions between them would lead to a CP violating term in the effective Lagrangian 1.1 [Pec08] [PQ77]. The problematic term 1.1 appears in the gluon field, and we will use the similarity between gluon and electromagnetic field in the following.  $\tilde{F}_{\mu\nu} = \epsilon_{\alpha\beta\mu\nu} F^{\alpha\beta}$  denotes the Hodge dual of a tensor. This term should be included for several reasons, one is the inclusion of all terms respecting the gauge invariance of the theory.  $\tilde{\Theta}$  is a combination of two contributions from the phase between the different vacuum states of the theory and a contribution from the quark masses.

$$L_{\text{CP}} = i\tilde{\Theta} \frac{g^2}{32\pi^2} F_a^{\mu\nu} \tilde{F}_{a\mu\nu} \quad (1.1)$$

The same expression  $F^{\mu\nu} \tilde{F}_{\mu\nu} \sim \vec{B} \cdot \vec{E}$  is in QED a product of a vector and an axial vector. In both cases, charge conjugation introduces a change of the sign, while parity leaves the axial vector  $\vec{B}$  unchanged. This results in a sign change under  $\hat{C}\hat{P}$ , with a potential for CP violation in interactions and requires a sign change under time reversal  $\hat{T}$  to keep  $\hat{C}\hat{P}\hat{T}$  conserved. This CP violation would lead to an electric dipole moment of the neutron proportional to  $d_n = 5.2 * 10^{-16} \tilde{\Theta} \text{e cm}$ . From measurements, it can be inferred that  $\tilde{\Theta} \lesssim 10^{-10}$  [[Tan+18], chapter 111.2.1]. There is no reason in the SM for this parameter to be small, since it is a phase and both contributions are independent. There are several possible ways this may be enforced, one example is the introduction of a additional symmetry, proposed by Peccei and Quinn in 1977 [PQ77].

### 1.2.2 The Peccei Quinn symmetry

One solution is to introduce a new chiral symmetry, which is broken on a sufficiently high energy scale  $f_a$ . The constant  $f_a$  is called the decay constant of the axion, in analogy to

the decay constant of the pion  $f_\pi$ . This gives a relation between the decay constants and masses of pions and axions in the limit of vanishing quark masses, shown in equation 1.2 [[Tan+18], chapter 11.2.1].

$$m_a \approx \frac{f_\pi m_\pi}{f_a} \approx 5.70(7) \frac{10^9 \text{GeV}}{f_a} \text{meV} \quad (1.2)$$

The expansion around the ground state results in a new boson, the axion, and a term to dynamically cancel the CP violating term 1.1. It also gives rise to several new interaction terms in the Lagrangian 1.3 [[Pec08], equation 22].

$$\mathcal{L} = \mathcal{L}_{\text{SM}} + \bar{\Theta} \frac{g^2}{32\pi^2} F_a^{\mu\nu} \tilde{F}_a{}_{\mu\nu} - \partial_\mu \partial^\mu a + \mathcal{L}_{\text{int}}[\partial_\mu \frac{a}{f_a} \Psi] + \xi \frac{a}{f_a} \frac{g^2}{32\pi^2} F_a^{\mu\nu} \tilde{F}_a{}_{\mu\nu} \quad (1.3)$$

The possible couplings are to the photon, in addition to other model dependent couplings. The coupling to the photon is shown in equation 1.4, with the coupling constant  $G_{A\gamma\gamma}$  and the electromagnetic field-strength tensor  $F^{\mu\nu}$  [[Tan+18], equation 111.4]. It is important to note that the coupling to photons is the result of an effective field theory. On a deeper level, they appear because of the axion decaying into a fermion-antifermion pair, annihilating in the next step to two photons. This process also enables a mixing with  $\pi^0$  and  $\eta$ .

$$\mathcal{L}_{A\gamma\gamma} = -\frac{G_{A\gamma\gamma}}{4} F_{\mu\nu} \tilde{F}^{\mu\nu} \phi_A = G_{A\gamma\gamma} \vec{E} \cdot \vec{B} \phi_A \quad (1.4)$$

A coupling to two photons is contained in all axion models. The interaction with fermions is given in equation 1.5, with a model-dependent coefficient  $C_f$  [[Tan+18], equation 117].

$$\mathcal{L}_{\text{Aff}} = \frac{C_f}{2f_A} \bar{\Psi}_f \gamma^\mu \gamma_5 \Psi_f \partial_\mu \phi_A \quad (1.5)$$

Usually, the Yukawa coupling constants are called  $g_{ae}$  and  $g_{a\gamma}$ , they already include the dependency on the scale  $f_a$ .

### 1.2.3 Current axion models

The original axion model has been ruled out, because the branching ratios for several decays into axions are larger than the current, experimental limits for these decays. Other axion models with  $f_a$  much higher than the electroweak scale are still possible. This is often achieved by using a more complicated symmetry group. Two of them are often quoted, they use a  $SU(2) \times U(1)$ . The very large values of  $f_a$  lead to very low masses and weak couplings of axions in these models, with a axion photon vertex present in all these models. Their description is very brief, because it only the axion mass and its coupling to photons and electrons is important for the phenomenology.

### The KSVZ model

The Kim, Shifman, Vainshtein, Zakharov model [[Tan+18], 111.2.2] solves the problem by introducing a new, heavy quark  $Q$  with  $m_Q \approx f_a$  as the only particle carrying the charge of the Peccei Quinn (PQ) symmetry and  $f_a$  much larger than the electroweak scale. The axion mass is given in this model by equation 1.6.

$$m_a \simeq 6.3 \left[ \frac{10^6 \text{GeV}}{f_a} \right] \text{eV} \quad (1.6)$$

The Yukawa coupling constant gets an additional scaling, related to the charge of the heavy quark  $Q$  and the masses of the up and down quark.

### The DFSZ model

The model by Dine, Fischler, Srednicki and Zhitnisky [[Tan+18], 111.2.2] is a model with two Higgs doublets and a new scalar field, with quarks and Higgs coupling to it. This gives rise to a multiplet of Higgs particles, some of them with electrical charge. The lightest Higgs is at 125 GeV, while all other parts of the multiplet are sufficiently heavy to evade detection at the LHC.

#### 1.2.4 Primakoff effect

The coupling to photons is very important for experiments to detect axions, as it is a common property in all axion models and enables a conversion between axions and photons inside strong magnetic fields. This process is called Primakoff effect and was derived 1966 [HAP66]. The original prediction was not done for axions, but for decay processes involving photons. The Primakoff effect leads to a relation between the decay width  $\Gamma$  for the process  $A \rightarrow B + \gamma$  and the cross section for the opposite direction  $B + Z \rightarrow B + \gamma' \rightarrow A$ .  $A$  and  $B$  are particles, while  $\gamma'$  is an off shell photon and  $Z$  a charged particle, usually a heavy nucleus. It is important to note that the off shell photon may also belong to an extended electromagnetic field. Equation 1.7 gives the cross section for the coherent production in a nuclear Coulomb field in the high energy limit and small scattering angles [[HAP66], equation 2.25].

$$\frac{d\sigma(B \rightarrow A)}{d\Omega_A} \simeq \frac{8Z^2\alpha |F(q^2)|^2 \Gamma(A \rightarrow B + \gamma)/m_A}{m_A^2 [1 - m_B^2/m_A^2]^3} \chi_{AB} \frac{\Theta^2}{[\delta^2 + \Theta^2]^2} \quad (1.7)$$

$\Theta$  is the angle between the momenta of particles  $A$  and  $B$ ,  $\delta \equiv \frac{1}{2}(m_A^2 - m_B^2)/E_B^2$  and  $|F(q^2)|$  is the form factor of the nucleus.  $\chi_{AB} \equiv \frac{\eta_B'(2S_{A+})}{\eta_B(2S_{B+})}$  contains the spin states  $S_A$  and  $S_B$  of the particles, while the  $\eta$  are dependent on the particle.

$\eta_B = \begin{cases} 1 & B \neq \gamma \\ \frac{1}{2} & B = \gamma \end{cases}$  and  $\eta'_B = \begin{cases} 1 & m_B \neq 0 \\ \frac{1}{2}(2S_B + 1) & m_B = 0 \end{cases}$  depend on the type of particle involved. The Primakoff effect, combined with the  $\gamma\gamma a$  vertex enables the conversion between photons and axions in electromagnetic fields, involving a second photon and an axion.

### 1.2.5 Solar axion production

In the dense, hot stellar cores, conversion of photons to axions may happen via different processes. The Primakoff effect is present in all axion models and creates a continuous spectrum. Since the energy is mostly provided by the real photon, the shape of the energy spectrum for small axion masses is very close to a black body spectrum. If the axion has a coupling to electrons, additional processes become possible. Their names are in analogy to the names of these processes involving photons. In figure 1.1 the Feynman diagrams for these processes are drawn. These reactions are often called ABC reactions, for Atomic-axio deexcitation, axio-Bremsstrahlung while scattering on electrons or ions and Compton scattering with emission of an axion. These processes compete with the photon emission in the same processes.

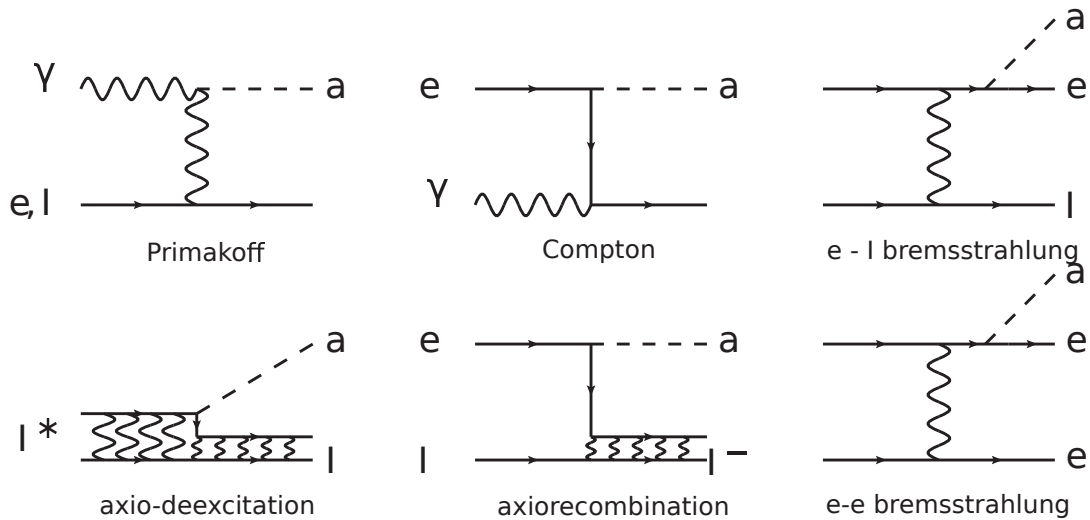


**Fig. 1.1:** Feynman diagrams for Primakoff and ABC axion production processes. I denotes ions. [[Red13], fig 1]

A combination of models for the sun and the cross sections for the different processes enables a calculation of the solar production of axions. The coupling constants for these interactions, as well as the axion mass, are unknown. In figure 1.2, the results of a simulation for solar axion flux are shown, assuming possible parameters for axion couplings and mass, as well as a solar model (AGSS09).

It is important to note the flux has several components and the couplings to electrons are not included in all models for axions or ALPs. Most axion flux is expected between 0.5 keV and 7 keV, defining the region of interest for the search of solar axions.

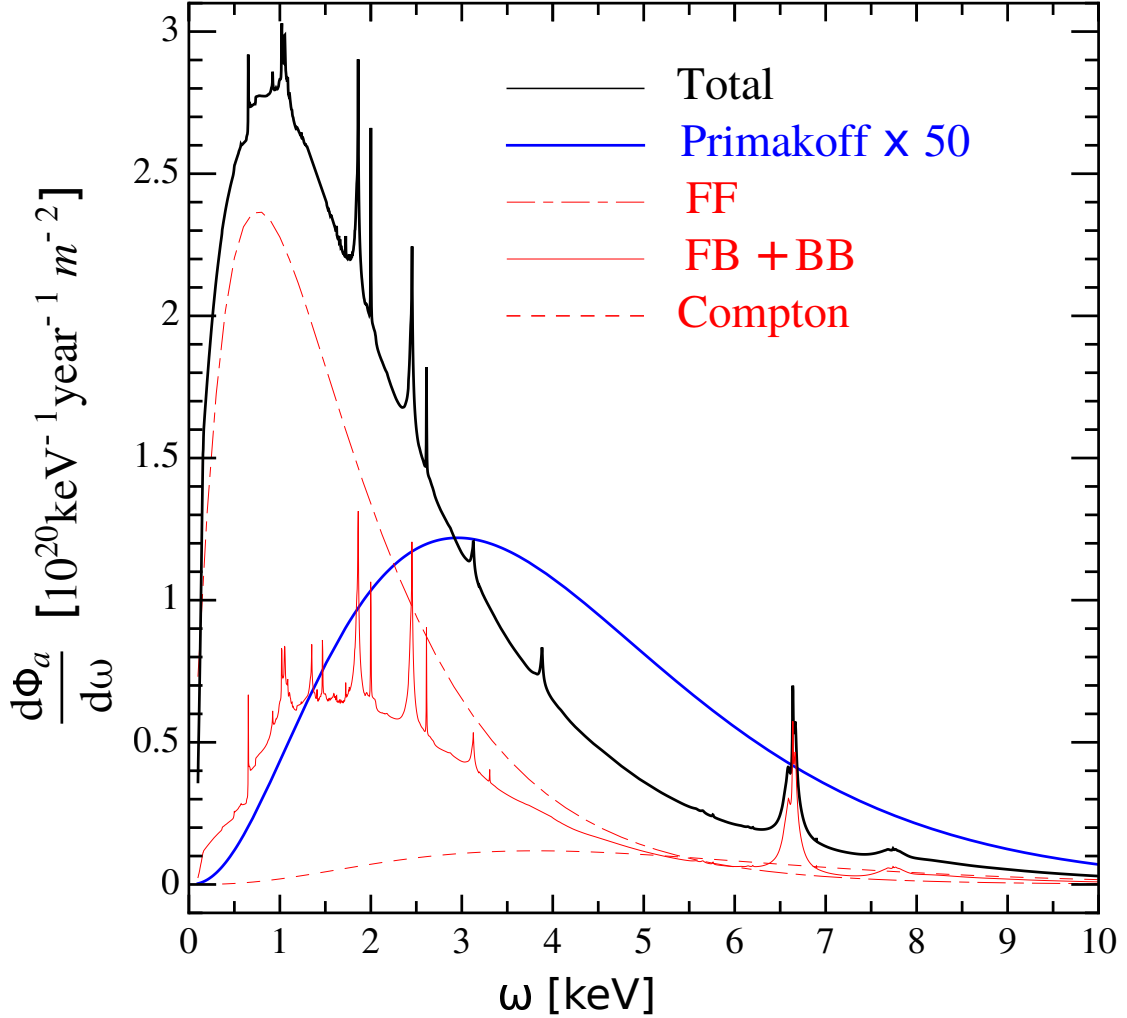


**Fig. 1.2:** ABC axion production processes, assuming coupling to electron and photon with  $g_{ae} = 10^{-13}$  and  $g_{a\gamma} = 10^{-12}$  with axion mass in the meV range. FF is bremsstrahlung and FB+BB atomic recombination and deexcitation [[Red13], fig 2].

### 1.2.6 Hints on the existence of axions

The parameter space for axion couplings and masses has been constrained by several experiments and observations. These can be grouped into astrophysical observations and laboratory experiments. Currently, some of the best limits are calculated by observations of

stellar populations and properties. The basic principle uses, that an additional energy loss by axions would cause stellar remnants to cool faster and shorten the lifetime of stars. Axions have been proposed as explanation for cooling anomalies of white dwarfs and other stellar remnants. Another way to test for axions is a comparison of the total neutrino flux, proportional to the power produced by fusion, to the luminosity of the star. Axion emissions would appear as an excess of neutrinos compared to the luminosity of the star, especially the sun. In figure 1.3, different hints and exclusion limits are shown. The IAXO would probe deep into a part of parameter space motivated by hints from stellar evolution. The zone labeled HB-hint refers to the horizontal branch in the Hertzsprung–Russell diagram, a region of older stars with a helium burning core. It is also interesting to note that all cooling anomalies and hints from stellar observation seem to indicate faster cooling rates than predicted ([Arm+19], page 39). Another type of hint is excessive X-ray emission by galaxies. These may be caused by the decay of axions or their conversion in the extended magnetic fields of these objects.

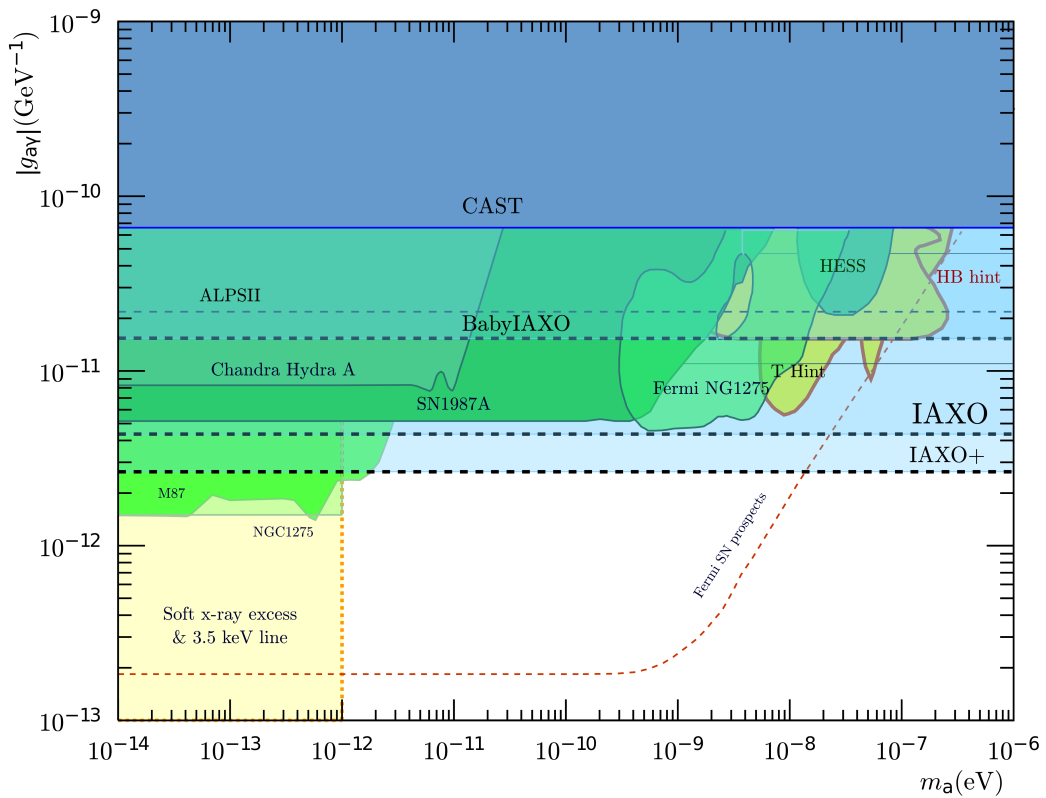


**Fig. 1.3:** Sensitive regions of several experiments and hints for axions in coupling and mass parameter space[[Arm+19], fig 14].



## 1.3 Detection of axions and ALPs

Several detection methods for axions have been proposed. One way to classify them is by the source of axions. Haloscopes try to detect the axions of the dark matter halo of our galaxy. Light shining through wall experiment like ALPs use strong lasers inside magnetic fields to produce axions and convert them back to photons after an absorber stopped all photons. A third option is using a helioscope to detect axions produced by the sun. This method is described in further details in the following, since it is important for this thesis.

### 1.3.1 Helioscopes

A helioscope is an instrument to observe the sun. In case of a helioscope for axions, the first step is a conversion of axions into photons in a strong magnet. In the next step, the converted axions are focused by X-ray optics on a detector sensitive to X-ray photons. In the following, each subsystem will be described with focus on IAXO and Baby IAXO. The efficiency of different experiments can be compared using several figures of merit (FOMs), defined for the different subsystems. The total FOM is the product of the FOMs of the different subsystems.

#### Tracking

Because the photons produced by the sun travel radially outward from the sun and the experiment has a limited field of view, it is necessary for the experiment to track the sun. Depending on the time of data taking  $t$  and the fraction of the day the sun can be tracked  $\epsilon_t$ , the figure of merit is defined in equation 1.8.

$$f_T = \sqrt{\epsilon_t t} \quad (1.8)$$

To maximize this FOM, a wide range of movement for the experiment is useful to keep the sun in focus for a large fraction of a day.

#### Magnet

Inside the magnet of the experiment axions are converted into photons by coupling to virtual photons of the magnetic field. This process is the inverse of the production via Primakoff effect, as described in 1.2.4. The FOM is defined in equation 1.9.

$$f_M = B^2 L^2 A \quad (1.9)$$

The FOM depends on magnetic field strength  $B$ , conversion volume length  $L$  and cross section  $A$ . For a large FOM, strength and size of the magnet bore containing the conversion

volume have to be as large as possible. For an increase in detection probability, helium may be introduced in the conversion volume to adjust the photon virtual mass to the axion mass. This increases the coherence length for the interaction between axions and photons and enables searches for axions with larger masses, as well as measuring the mass. This is accomplished by variation of the gas density, leading to a change in the index of refraction. This changes the speed of photons inside the conversion volume. If the speed for photon and axion are the same, the conversion probability is maximal. It should be noted that this FOM can be calculated by integrating the magnetic field in two or three dimensions, but this requires precise knowledge of the field strength map.

### Optics

To reduce noise and detector size, a X-ray optic focuses down from the conversion volume cross section  $A$  to a spot size of  $a$ . The optics have a throughput  $\epsilon_O$ , since some photons may be lost during focusing by absorption. For both IAXO and Baby IAXO, focal ranges around 5 m are planned. The FOM is defined as in equation 1.10.

$$f_O = \frac{\epsilon_O}{a} \quad (1.10)$$

These optics are usually build using glass substrates and use grazing (or glancing) reflections, where the photons have an angle of only a few degrees relative to the mirror surface. The mirrors are usually coated with multi-layer systems of high  $Z$  and low  $Z$  materials to achive higher reflectivity. Many concentric shells of mirrors are combined to collect and focus larger cross sections. This kind of optics is also used in X-ray telescopes on satelite missions.

### Detector

The detector has several requirements that differ from the detection in accelerator experiments. A very important difference is the expected energy of the axions, usually in the keV range, compared to the usual cuts at the GeV scale in experiments like ATLAS. The event rates are also much lower, giving rise to an enviroment where background reduction and sensitivity are important. Currently, time projection chambers (TPCs) are often used because of low background rates and good energy resolution. The background rate has the dimension  $[b] = \frac{1}{\text{keV cm}^2 \text{ s}}$  and the detection efficiency is  $\epsilon_D$ . The FOM is defined in 1.11.

$$f_D = \frac{\epsilon_D}{\sqrt{b}} \quad (1.11)$$

### External radiation

External radiation is caused by different sources. Low energy ionising radiation caused by radioactive decays can be shielded, while energetic photons require several centimeters of

lead for sufficient reduction. Layers of hydrocarbons may be used to moderate neutron radiation and stop charged particles without generation of bremsstrahlung. Against cosmic radiation, especially muons, shielding is inefficient because of the high energies and the behaviour as minimal ionising particle (MIP). Against this component of the external radiation, a veto around the detector is used. This is especially important, since the energetic particles may induce characteristic X-rays in the construction materials. This radiation may be reduced using veto counters to reject events associated with external radiation.

**Internal radiation** Additional radiation is caused by radioactive materials inside the shielding, for example  $^{14}\text{C}$  and other isotopes in the construction materials. These decays may produce directly X-rays or excite the characteristic lines of other atoms. This characteristic radiation is inside the region of interest (ROI), usually in the range of 1.5 keV for aluminium to 8 keV for copper. It is important to reduce this radiation by avoiding radioactive materials inside and near the detection volume, as well as upstream from the detector in the optics and magnet. This requires the use of radiopure materials and measurements of the internal radiation, for example in an underground laboratory.

### 1.3.2 Comparison between current and future helioscopes

I will compare a current helioscope, CERN axion solar telescope (CAST), to both IAXO and Baby IAXO, with most focus on the factors that increase the FOM. The parameters important for the FOM are summarised in table 1.2, while the influence on their sensitivity for axions with different mass and coupling constant is shown in 1.6.

#### CERN axion solar telescope

As of 2020, the axion helioscope of the highest FOM is CAST, using a LHC dipole magnet of 9.26 m length at 9.0 T field strength. Because of the magnet design for a proton collider, the magnet has two beam pipes and an aperture of only 43 mm diameter for each beam pipe. The tracking time of the sun is 1.5 h per day on both sunrise and sundown side, or 12.5 % of a day, because of a limited range of movement for the altitude. The throughput of the optics is at 0.3 with 15 m focal range using a Wolter type-1 telescope originally developed for NuSTAR. There are four detection setups, at both ends of each beam pipe observing the sun during sunrise and sundown. The detectors changed over time, including MicroMESH Gaseous Structure (MICROMEGAS), charge-coupled device (CCD), silicon drift detector (SDD) and InGrid [Ira+13].

### Baby IAXO

Baby IAXO is planned as a smaller scale test in preparation of IAXO with a potential for axion discovery. The most important change compared to CAST is the purpose build magnet as a racetrack configuration. The magnet will use NbTi superconductor in copper, operating at 9.8 kA and 3.2 T peak field, with an average field of 2 T. Inside the magnet, two conversion tubes of 700 mm diameter enable a much larger collection area compared to previous experiments. The range of movement is also much larger, using a telescope mount for a medium-sized telescope (MST) of the Cherenkov Telescope Array (CTA). This enables a superior range of movement compared to CAST, requiring only one set of detectors and X-ray optics for each of the conversion tubes. Both tubes will be equipped with X-ray telescopes with focal range around 5 m. Currently it is planned to use one purpose-build telescope as preparation for IAXO, while the second tube will use a spare optic of XMM Newton. For detection of x-ray photons, InGrid chips are planned, with the option to use other detection methods like SDD or Transition Edge Sensor (TES) at the focal spot.

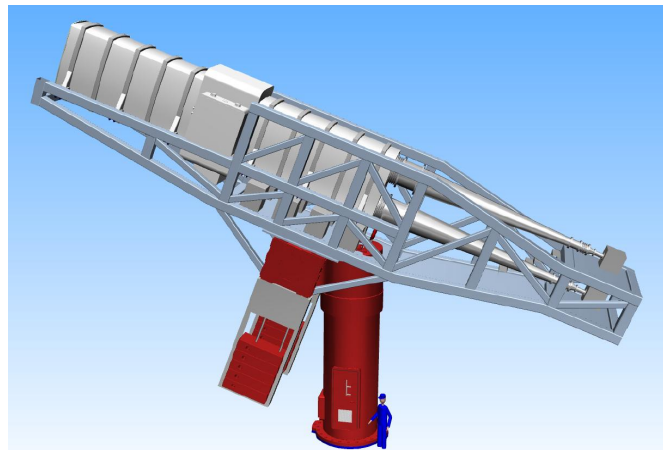


**Fig. 1.4:** Schematic view of the Baby IAXO experiment, mounted on CTA platform. In the experiment, one detection line will be shorter, because of the different optics used. [Col19]

As shown in the plots of the axion parameter space, even at the Baby IAXO stage a detection of axions is possible.

### International Axion Observatory (IAXO)

IAXO will use the experiences learned in Baby IAXO to reach much higher sensitivity. The most visible difference is the shape of the magnet system and subsequent number of optics

and detectors. This is because the magnet is build similar to the toroid magnet of the ATLAS experiment with eight racetrack coils generating an average magnetic field of 2.5 T. The magnet will use NbTi superconductor inside a copper matrix at a current of 12.3 kA and a peak field of 5.4 T. For an efficient use of available space, the conversion tubes of 600 mm diameter are placed between the coils. Each tube has a separate X-ray optic and pipe to focus the signal on a detector. The types of detector are the same as for Baby IAXO, with increased performance and reduced background as result of ongoing research.[Ira+13]

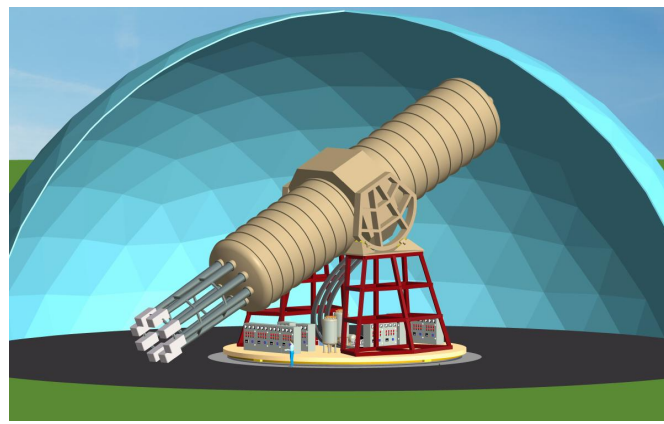


**Fig. 1.5:** Schematic view of the IAXO experiment. The eight detection lines with detectors are visible. [Ira+13]

### Summary of helioscope performance

In table 1.2, the FOM of the described helioscopes are compared. Very large improvements are expected in background and magnet performance by using larger and stronger magnets, as well as lowering the background. In figure refHelioskopSensi the parameter space that can be probed by different experiments is shown.

Parameter	Units	CAST	Baby IAXO	IAXO	IAXO upgraded
B	T	9	2	2.5	3.5
L	m	9.26	10	20	22
A	m <sup>2</sup>	2x0.0015	2x0.38	2.3	2.3
f <sub>M</sub>	T <sup>2</sup> m <sup>4</sup>	20	230	6000	24000
F <sub>m</sub> <sup>*</sup>		1	11	300	1200
ε <sub>O</sub>	cm <sup>2</sup>	0.3	0.35	0.7	0.7
a		0.15	2x0.3	8*0.15	8x0.15
f <sub>O</sub> <sup>*</sup>		1	0.6	2.3	2.3
ε <sub>D</sub>	$\frac{10^{-5}}{\text{keV cm}^2 \text{ s}}$	0.5-0.9	0.7	0.8	0.8
b		4	10 <sup>-2</sup>	10 <sup>-3</sup>	10 <sup>-4</sup>
f <sub>D</sub> <sup>*</sup>		1	20	70	230
ε <sub>t</sub>	year	0.12	0.5	0.5	0.5
T		1	1.5	3	5
f <sub>T</sub> <sup>*</sup>		1	2.5	3.6	4.6
f <sup>*</sup>		1	330	174000	2920000

**Tab. 1.2:** Performance of current and planned helioscopes in comparison. f<sup>\*</sup> denotes relative FOM normalised to CAST. Data from [Ira+13] and [Arm+19].

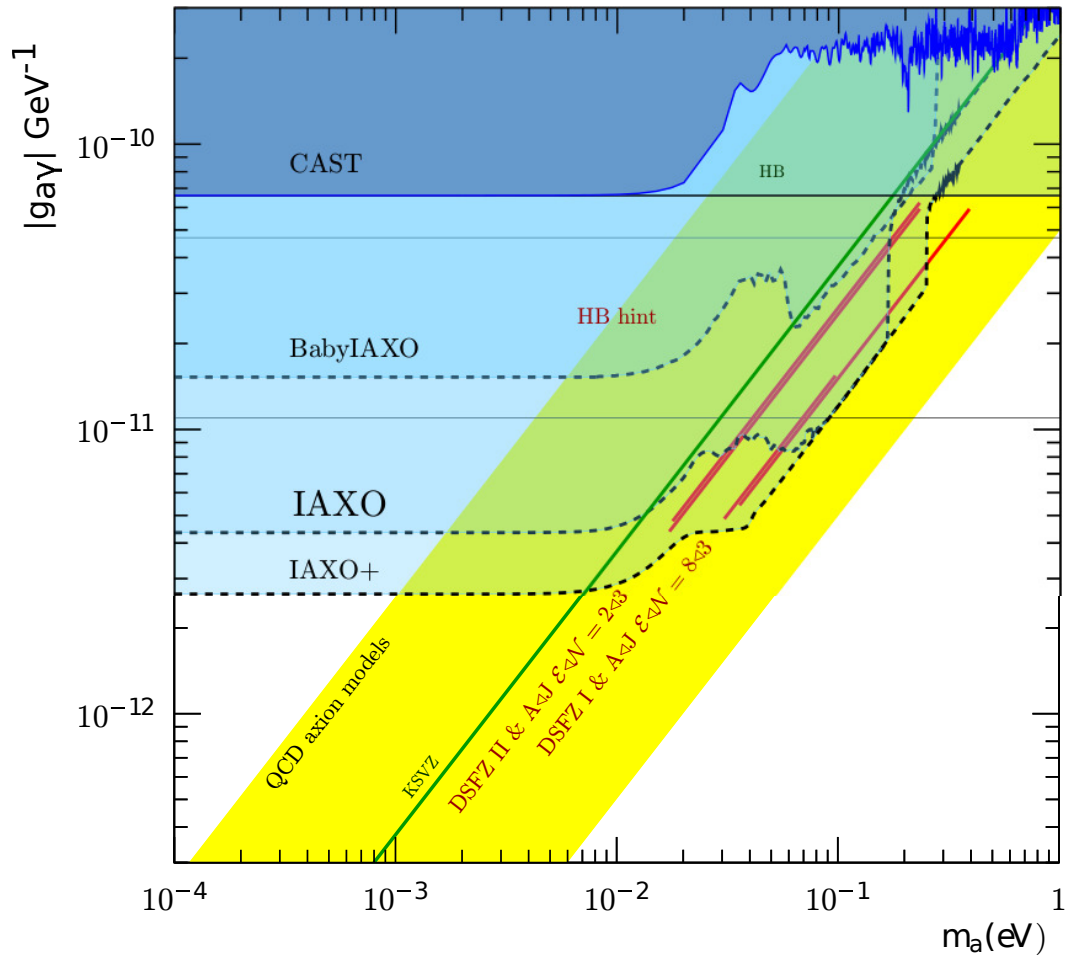


**Fig. 1.6:** Sensitivity to axions for several helioscope experiments, as well as some hints from other observations and the region motivated by QCD axions. [[Arm+19], figure 10]





## Theoretical background of gaseous detectors

Gaseous detectors are used in different experiments, especially if tracking of charged particles is required, little material is to be used and moderate rates are expected. Usually, the process of detection can be split into several, distinct steps. The first step is the generation of charge carriers inside the gas by interactions of the particle to be detected. After this, charge carriers diffuse in the gas and drift in the electromagnetic fields inside the detector. At the end, they reach the amplification and readout to be detected. For efficient use of gaseous detectors, each of these steps is important and has to be understood.

### 2.1 Generation of charge carriers

The first step in detection of particles in a gaseous detector is the generation of free charge carriers. The exact mechanism depends on both energy and involved particles. For charged, fast particles the Bethe Bloch formula is a good approximation over wide energy ranges. In case of neutral particles like photons the first step often transfers part or all momentum on an electron or atom, which in turn causes further ionisation.

#### 2.1.1 Bethe Bloch formula

The Bethe Bloch formula describes the energy loss of charged particles in matter. In the case of electrons, there apply additional corrections because both partners in the scattering processes involved are indistinguishable. The energy loss per distance traveled  $\frac{dE}{dx}$  is dependent on the charge of the fast particle  $z$ , as well as its velocity as a fraction of the speed of light  $\beta = \frac{v}{c}$  and the Lorentz factor  $\gamma = \frac{1}{1-\beta^2}$ . For the target material,  $Z$  and  $A$  are atomic number and weight, with the density  $\rho$ .  $N_A$  is Avogadro's number,  $r_e$  the classical electron radius and  $I$  is the mean excitation energy of the target material. The Bethe Bloch equation

is shown in equation 2.1.

$$\frac{dE}{dx} = 4\pi N_A r_e^2 mc^2 \rho z^2 \frac{Z}{A} \frac{1}{\beta^2} \left[ \ln\left(\frac{2mc^2\beta^2\gamma^2}{I}\right) - \beta^2 \right] \quad (2.1)$$

It should be noted that the Bethe Bloch formula only calculates the average energy loss. The number of charge carriers per distance shows fluctuations.

### 2.1.2 A different look at the ionisation

The energy transfer between a fast particle and matter involves different forms of energy loss. Parts of the energy loss create free electrons, in some cases with enough energy to cause further ionisation or even travel some distance and be observed as a  $\delta$  or knock-on electron. Energy may also be deposited in form of excitation of bound electrons and in turn reemitted as photons or transferred in collisions. Another option is the transfer of momentum and energy in elastic collisions. Of these different forms of energy deposition, only those capable of causing free charge carriers are important for the signal. The ionisations are split between primary ionisation, caused directly by the energetic particle, and secondary ionisation caused by sufficiently energetic primary electrons or energy transfer from excited atoms. It is important to note that the ionisation energy and the average energy needed to generate a electron ion pair are different, since some of the energy is lost to other processes. Most of these processes become more important at higher energies, thus they are of little relevance in this thesis.

### 2.1.3 Ionisation by X-rays

Since photons are not charged, they do not lose energy according to the Bethe Bloch equation. Instead, they interact with charged particles via different processes. For low energies, the process is usually just scattering without energy loss or excitation of electrons to higher energy states inside the electron shell of atoms. With more energy, ionisation and transfer of the energy of the photon to an electron is important. The electron then may lose the energy gained by ionisation of other atoms. This process transfers the whole energy of the photon, except the energy needed to ionise, to the electron. For even higher energies, inelastic scattering in the Compton effect contributes, causing the photon to transfer part of its momentum to the electron. At even higher energies, above 1 MeV, pair production can start, generating electron positron pairs from high energy photons. In context of this thesis, only photo effect is relevant, since the energies are below 100 keV.

### Escape peaks

An important feature of X-ray spectra is the presence of escape peaks. They appear at lower energy and with less strength than the main peak and are caused by energy leaving the detection volume. This happens when the ionisation in a lower shell of an atom has caused a vacancy and this is filled by an electron from a higher shell falling to a lower energy state and emitting the energy difference as photon. If this photon is not absorbed inside the detection volume, a lower energy is detected. Most often this involves a hole in the K-shell getting filled, the energy of the escaping photon can be calculated using the Rydberg formula 2.2. The formula is often given using the frequency or wavelength, for the purposes in this thesis the form with energy and for hydrogen like elements is used.

$$E = 13.6 \text{ eV} * Z^2 \left( \frac{1}{n^2} - \frac{1}{m^2} \right) \quad (2.2)$$

The appearance of escape peaks is an effect of the detector material. For the context of this thesis, the important escape peak is caused by argon, with a shift of approximately 3 keV.

### X-ray photons of Fe-55

The isotope Fe-55 is often used for calibration purposes. It decays via electron capture, involving an electron from the 1s or 2s orbital and producing Mn-55. This leaves the electron shell in an excited state. Subsequent deexcitation can happen via Auger electrons or emission of x-ray photons. Auger electrons are the result of a deexcitation by transferring the energy to an electron in the shell. This results in the emission of electrons with several characteristic energies. The range of these electrons is usually very short. The photons are emitted as several, closely spaced lines around 5.9 keV.

#### 2.1.4 Intense LASER beams

To generate straight lines of ionisation, a pulsed, short wavelength LASER beam can be used. Even in the ultra violet (UV) range, individual photons have only several electron volt (eV) energy. For example, a 250 nm photon has approximately 5 eV, much less than the ionisation energy of most molecules and noble gases. For a successful ionisation, several photons have to be absorbed faster than the deexcitation happens. In this case, the electron is excited to several very short lived energy states until the energy exceeds the ionisation energy.

Because this ionisation process takes several photon absorptions, it is more likely in the intense photon flux of a pulsed LASER. In this case, the rate of ionisation  $R$  follows equation 2.3, which is proportional to the number density of molecules per volume  $N$  and the volume

affected by the beam  $V$ . It is also dependent on the cross section for a photon absorption  $\sigma$  and the photon flux  $\Phi$ .

$$R = NV(\Phi\sigma)^n \quad (2.3)$$

The original molecule is as a result often fragmented.

## 2.2 Behaviour of free charge carriers in gas

The free charge carriers generated by ionisation are electrons and charged ions.

In an electrical field, the charged molecules or electrons experience a Lorentz force depending on their charge and the electromagnetic field.

$$\vec{F} = q(\vec{v} \times \vec{B} + \vec{E}) \quad (2.4)$$

In addition to the constant acceleration in the electromagnetic field, interactions with gas molecules affect the drifting charge carriers. Most of these interactions are collisions, which are elastic or inelastic depending on the energy and the collision partners. This gives rise to the drift in the electrical field, diffusion and Townsend avalanche. The exact behaviour is dependent on the gas composition, its density and the type of charge carrier, as well as the field strength. The different regimes of drift are explained in detail in the next sections, with a focus on electrons.

### 2.2.1 Drift in electrical fields

If the electrical field is sufficiently weak, they gain little energy on the mean free path between two collisions. Because of the low energy, these collisions are elastic and just transfer momentum from the drifting charge carrier to the gas molecules. The effect of these collisions can be approximated as a force proportional to the drift velocity  $\vec{u}$  with a constant  $K$ . This can be combined with the equation refLorentzForce for the Lorentz force to the equation of motion for a drifting charge carrier 2.5.

$$m \frac{d\vec{u}}{dt} = q(\vec{E} + \vec{u} \times \vec{B}) - K\vec{u} \quad (2.5)$$

The ratio  $\frac{m}{K} = \tau$  has the dimension of a characteristic time between two collisions with gas molecules and is dependent on the parameters of the gas and the charge carrier in question. In the following sections,  $\vec{B} = \vec{0}$  is assumed. If the observed time scale is much larger than the mean time between interactions, the charge carriers seem to drift with an average velocity according to equation 2.6.

$$\mu = eK = \frac{e\tau}{m} \quad (2.6)$$

In a more detailed picture, the charge carriers have a velocity distribution, depending on the cross section for the interaction, average energy loss in the collision, field strength and gas density. Often, the density and the electric field strength are combined to the reduced electric field according to 2.7 and the dimension of Townsend.

$$\frac{[E]}{[N]} = Td = 10^{-17} \text{V cm}^2 \quad (2.7)$$

### 2.2.2 Diffusion

In the collisions, the charge carriers interact with gas molecules and exchange energy and momentum. In absence of electromagnetic fields, this would result in a random walk. This would result in a diffusion that is isotropic in all directions. In the presence of an electrical field, a additional force is imposed on the charge carriers by the Lorentz force 2.4. The energy dependence of scattering processes causes in this case an anisotropic diffusion.

#### Diffusion without fields

If there is no external electromagnetic field imposing additional forces on the charge carriers, the diffusion for charge carriers injected at  $r = 0$  at  $t = 0$  follows equation 2.8, a three dimensional Gaussian.

$$n(t, \vec{r}) = \frac{1}{(\sqrt{4\pi Dt})^3} \exp\left(-\frac{r^2}{Dt}\right) \quad (2.8)$$

In this equation,  $D$  is the diffusion constant and  $n$  the probability for an electron.

#### Diffusion with electrical field

In the presence of an electrical field, the constant acceleration by the Lorentz force imposes a preferred direction of motion on the charge carriers. Since cross section and other scattering parameters are energy dependent, this causes a difference between longitudinal diffusion in direction of the field and transversal diffusion perpendicular to the field. The diffusion constant for the different directions is indicated by an index  $T$  for transversal and  $L$  for longitudinal. Assuming the field is in  $z$  direction, the diffusion follows equation 2.9.

$$n(t, \vec{r}) = \frac{1}{\sqrt{4\pi D_L t}} \frac{1}{(\sqrt{4\pi D_T t})^2} \exp\left(-\frac{x^2 + y^2}{4D_T t} - \frac{(z - ut)^2}{4D_L t}\right) \quad (2.9)$$

Note that the center of the charge cloud is moving with the drift velocity  $u$  in direction of the electric field.

### 2.2.3 Charge multiplication by Townsend avalanche

In a sufficiently strong electric field, the charge carriers can gain sufficient energy to eject electrons from the hull of neutral gas atoms. This process liberates additional charge carriers, which can lead to an exponential increase in the number of charge carriers. This amplification process is referred to as a Townsend discharge or Townsend avalanche. The first Townsend coefficient  $\alpha$  in equation 2.10 is a function of the gas mixture and the reduced electric field.

$$dN = \alpha N ds \quad (2.10)$$

Combined with the initial number of charge carriers  $N$  and the distance traveled  $ds$ , the Townsend equation implies an exponential increase in charge carriers during amplification.

### 2.2.4 Difference between different charge carriers

The different charge carriers in a gas are free electrons, as well as positive and negative charged molecules or ions. Between electrons and ions is a huge mass difference of at least three orders of magnitude. This leads to differences in the maximal energy transfer in collisions with gas molecules and acceleration in the field. The main effect is a much lower drift velocity  $u$  for ions compared to electrons. For the same reasons, the contribution of ions to charge multiplication is only a small contribution.

### 2.2.5 Gas impurities

Trace compounds in the gas mixture may have several effects, depending on the conditions inside the chamber and the nature of the impurities. Especially with organic quenchers like methane and high rate environments, polymerisation reactions may cause deposits on electrodes. Impurities may also capture electrons and form negative ions. Since ions have only a small contribution to charge multiplication, compared to electrons, these charge carriers are usually lost of the signal. Examples for this are oxygen or water. Minimising and knowledge of these losses is important for measurement of energy deposits in the gas, for example for measurement of  $\frac{dE}{dx}$  for the identification of charged particles.

## 2.3 Readout of drift chambers

Drift detectors usually have a sensitive volume, filled with the gas mixture and an electric field for drifting the electrons to the readout. Before the readout, a strong electric field may cause an amplification of the signal by Townsend avalanche, followed by a readout system converting the charge signal into the desired form. The amplification by an avalanche inside

the gas is beneficial because high amplifications are possible without introducing electronic noise by amplifiers at this stage. This leads to an increased signal to noise ratio.

### 2.3.1 Amplification

For amplification, different techniques exist. In the past, multi-wire proportional chamber (MWPC) were often used. More recently, micropattern gas detector (MPGD) are often employed to amplify the signal. In case of MWPC, many thin wires cause electrons in their vicinity to generate an avalanche, which is then collected on the wire. Additional wires in the vicinity enable a reconstruction of the particle track by using arrival times and distribution of the signal between different wires.

In the case of MPGD, the avalanche is usually constraint in the lateral expansion by the structure of the MPGD. For example, in a gas electron multiplier (GEM), the holes in an insulator limit the expansion of the avalanche, while conductors on both sides of the insulator generate a field for amplification. The limited lateral expansion of the avalanche makes a better position resolution possible. Depending on the type of MPGD, several amplification stages may be stacked. In first approximation, the resulting amplification is the product of the individual amplifications. Other concepts build the amplification stage directly on top of the readout, removing diffusion between the different amplification stages and limiting the lateral extension of the signal even further.

### 2.3.2 Readout using charge sensitive amplifier

The signal after amplification is a cloud of charge carriers in the gas. This charge can be collected on conductive surfaces and amplified using charge sensitive amplifier (CSA) as a first stage. Usually, this first stage is followed by additional electronic amplifiers and shapers until the signal is converted to a digital format and stored.

### 2.3.3 Readout using Timepix 2

The Timepix application-specific integrated circuit (ASIC) is derived from the Medipix 2 chip. It is manufactured in  $0.25\mu\text{m}$  6 metal complementary metal-oxide-semiconductor (CMOS) technology ([Cud07], page 17) with a pixel size of  $55\mu\text{m} \times 55\mu\text{m}$  and  $256 \times 256$  pixels. An internal clock signal is generated by the chip for time measurement inside the pixels and the shutter signal. Only while the shutter is open, the chip accepts signals. Each pixel consists of an analog and a digital section. The analog section contains both CSA and discriminator including the threshold adjustment. The digital part contains the control logic of the cell, as well as the 14-Bit register for counting during chip operation. In the analog part, the threshold consists of a threshold adjustment to equalize the threshold of

all pixels and a global threshold referred to as THL. A capacitance can be connected using the Testbit to enable injection of charge into the amplifier for calibration purposes. The Maskbit can disconnect the analog and digital part of a pixel from each other, disabling the pixel. The digital part handles the communication and operation of the pixel. The Timepix Synchronisation Logic stores the setting for the individual pixel. This contains the settings for Testbit, Maskbit, as well as p0 and p1 for the pixel mode and the threshold equalisation. The other components are the register for counting and additional components for communication and operation of the pixel. Details about them are available for example in [Cud07].

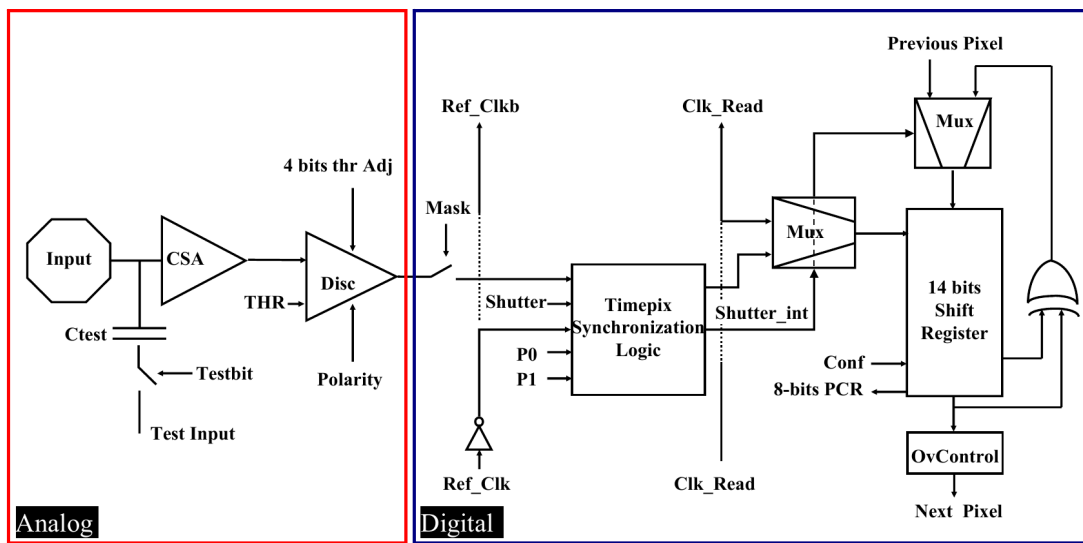


Fig. 2.1: Schematic layout of a Timepix pixel [[Cud07], page 100].

For the operation of the Timepix chip p0, p1, THL and threshold equalisation are especially important and will be explained in more detail.

p0 and p1 are used for choosing the operating mode of a pixel. The four possible combinations correspond to the four operation modes: 1Hit, Medipix, time over threshold (TOT) and time of arrival (TOA). In 1Hit mode, it is just checked if the threshold was exceeded. This mode is similar to Medipix mode, which counts how often the threshold was exceeded. In TOT mode, the pixel counts how many clock cycles the signal of the CSA was above the discriminator. This time has a linear relation to the input charge. The fourth mode is the TOA mode. It counts the time between the CSA exceeding the threshold and the end of shutter. It can be used to determine timing information of signals. Threshold equalisation is generated during the calibration of the chip to equalize the threshold between different pixels to have a homogeneous response of the chip. The threshold THL is the global threshold



for all pixel cells. This controls the minimal amount of charge needed for a pixel to react.

### 2.3.4 Readout using InGrid

InGrid is a combination of MPGD and Timepix chip. The first InGrid chips were manufactured in 2007. On top of a Timepix chip a series of insulating pillars suspends a metal grid. This grid is used to generate a strong electric field above the chip surface for amplification. The short distance between grid and chip limits the avalanche in transversal size. By matching the holes in the grid to the pixel of the Timepix chip, the avalanche is read out by a single pixel. This setup enables the detection of single electrons with high efficiency ([Fra12], page 87), compared to the approximately 650 electrons for a bare Timepix chip ([Cud07], page 113). These features enable a much finer resolution compared to the detection using GEM for amplification and Timepix chip for readout. An example is shown in figure 2.2, showing an event in an Ingrid chip and an event after amplification by three GEM layers and readout by a Timepix chip. The InGrid displays the substructure of the event, while the GEM and Timepix combination loses most of this information during the amplification in the GEM.

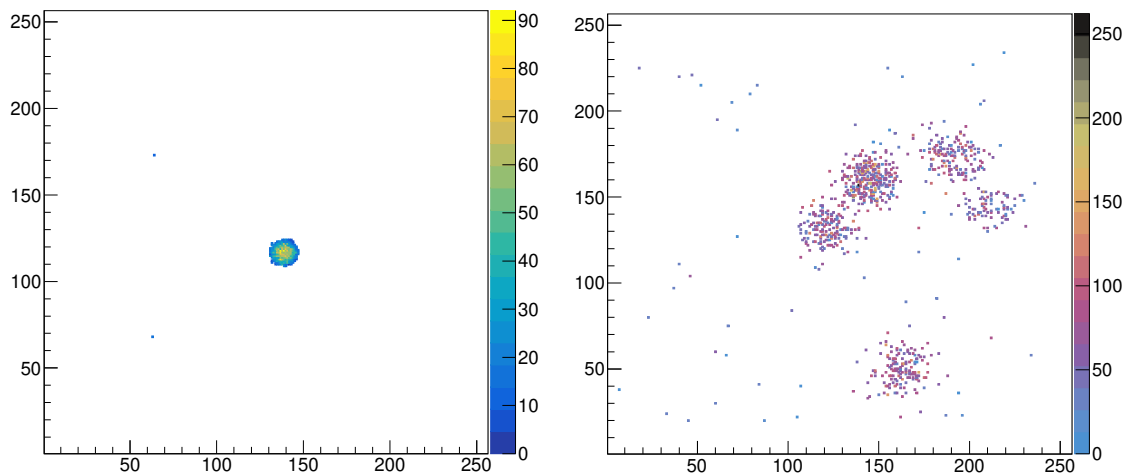


**Fig. 2.2:** Comparison of an event in the test chamber in Siegen with triple GEM for amplification on the left and an event in detected using an InGrid chip on the right.

### Manufacturing of InGrid

In the first step a Timepix chip is covered with a  $4 - 8 \mu\text{m}$  thick silicon nitride protection layer. In the next steps, a  $50 \mu\text{m}$  thick layer of SU-8 photoresist is applied and exposed to create the pillars to carry the grid. A  $1 \mu\text{m}$  thick layer of aluminium is deposited by

sputtering in several steps. On top of the aluminium layer, another layer of photoresist is deposited and exposed to create the mask for the holes of the grid. The photoresist is used as a mask to etch the holes in the aluminium layer. In the next steps, wafer is diced into the individual chips and the unexposed photoresist is removed ([Kri12], page 38). This is schematically shown in figure 2.3. The effect of the protection layer is to prevent damage to the chip during discharges by creating a high resistivity layer. The effects are investigated in ([Fra12], chapter 5).

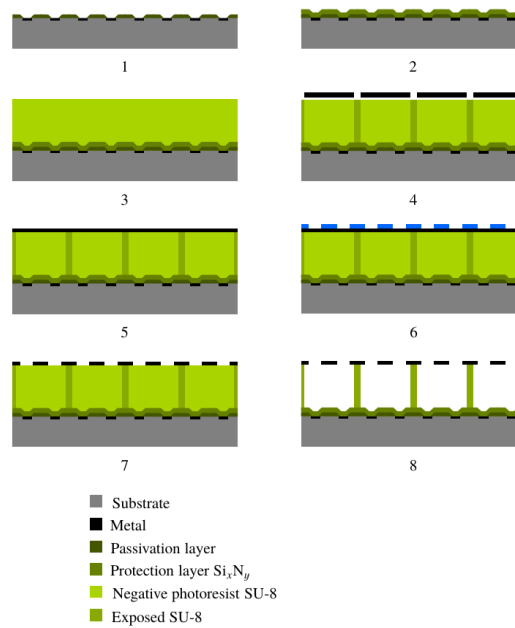


**Fig. 2.3:** Process steps for fabricating an InGrid on top of a Timepix chip by photolithographic postprocessing [[Kri12], page 40].

## Experimental setup

This section describes the hardware used in the setup at the University of Siegen. The setup consists of a small test chamber and its support infrastructure. The support infrastructure has a gas mixing system, high voltage supplies and means to generate test signals inside the chamber, as well as monitoring of gas temperature and pressure.

### 3.1 Gas supply

The gas mixture used is Ar:CO<sub>2</sub> in a ratio of 80:20. The gas supplied is argon 5.0 at 300 bar and carbon dioxide 2.2 at 200 bar nominal pressure. After reduction to less than 5 bar, the separate gases are supplied to the mixing station. A second pressure reduction valve lowers the pressure further to 2 bar before the mass flow meters of type MKS 247. The flow control adjusts the gas flow and generates the gas mixture at up to 200  $\frac{\text{sccm}}{\text{min}}$  per component. After the flow control the two gas streams are combined and proceed to the distribution panel. On the distribution panel, gas mixture or dry air can be supplied to the chamber and the flow rate adjusted by flow control valves after the shutoff valves. It is also possible to direct gas mixture directly to the gas monitor. From the distribution panel, the flow is directed to the chamber. The used gas flows back to the distribution panel and can be vented outside the building directly or after passing the gas monitor. Back-flow is prevented by glycerol filled bubblers. While not in use, the dry air is directed to chamber and monitor to avoid moisture. A sketch, omitting pressure gauges and cables, is shown in figure 3.1.

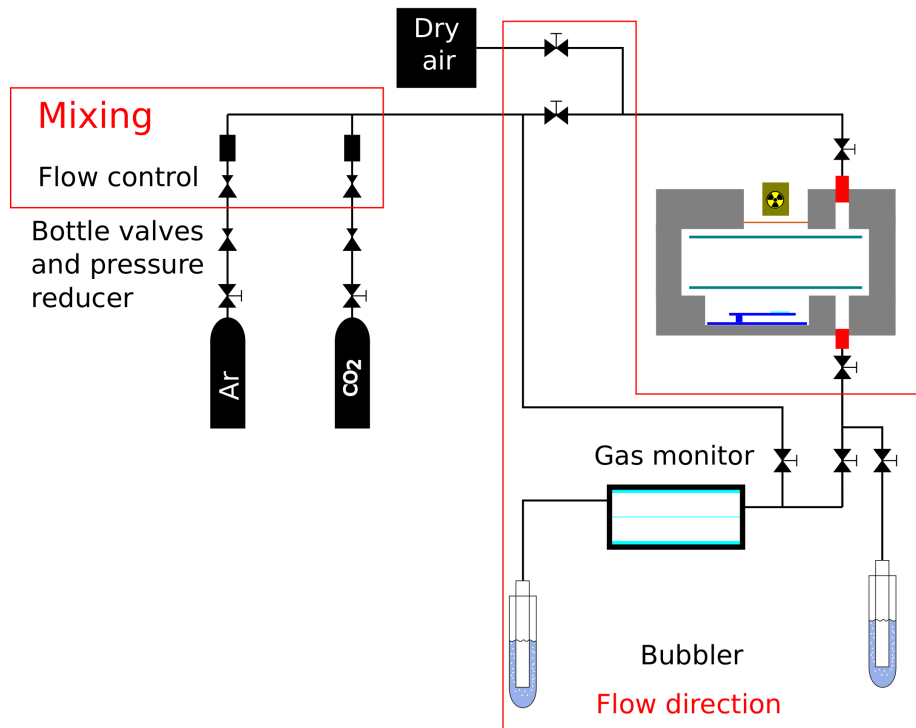


**Fig. 3.1:** Schematic of the gas system. Flow reduction valves on distribution panel and GEM chamber not shown.

The pipes used are stainless steel for rigid pipes and polyurethane for the flexible pipes.

### 3.1.1 Gas monitor

The gas properties can be monitored using a proportional counter irradiated by a  $^{55}\text{Fe}$  source. The gas flow may be directed into the monitor before or after passing through the detector. The signal of the proportional counter is amplified by an Ortec 672 and read out by a multi channel analyzer (MCA), while the operating voltage is supplied by a Silena Milano 7712. The peak position is dependent on the gas amplification inside the counter, which in turn is dependent on the amplification properties of the gas. This is used to check for a stable gas composition inside the detector, especially during the initial flushing with gas mixture to replace the air inside the detector.

### 3.1.2 Pressure control

An Arduino based control system can be used to increase the pressure relative to the external pressure. This device is usually placed after the chamber as part of the return pipe. It operates by observing the pressure inside a small sensor box and opening a magnet valve

if the set value is exceeded, until it undershoots and the valve is closed. This leads to periodic pressure oscillations around the set value, dampened by the restrictor valves of the distribution panel and the volume of the system. This enables an increase in pressure inside the system, at the cost of smaller, periodic changes in pressure.

## 3.2 IAXO test chamber

This section will describe the design and used materials of the test chamber, as well as some experimental parameters. The chamber was designed within the scope of this thesis. It is manufactured with a short distance between window and cathode to reduce losses of signal before reaching the sensitive volume, as well as valves to isolate it from the gas system.

### 3.2.1 Chamber layout

The main body of the chamber is manufactured from aluminium and polyvinylchloride (PVC). For better access and ease of changing parts, the chamber is built out of several segments. The main parts are the lid, base and frame. The frame consists out of 4 plates, fixed with steel M3 screws and cylinder pins for alignment. Sealing between these parts is achieved using “Würth Flächendicht grün“, a dimethacrylic acid ester. This frame has two cylindrical holes for radiation windows, fixed with M3 screws. On top and bottom of the frame is a groove for the rubber seal, sealing the connections to lid and base. Eight steel screws secure both lid and base to the frame, using M5 screws for the base and M3 for the lid. Both lid and base carry a valve and connector to the Festo pipes used in the gas system. On the lid one safe high voltage (SHV) connector enables connection to the cathode and a large window is present for the X-ray source. The base has a more complicated structure manufactured out of PVC, containing two SHV to connect to InGrid and anode. An additional opening with treads connects to a pocket in the base, for installation of the pressure sensor. The chip itself is placed at the center of the chamber and its carrier printed circuit board (PCB) is fixed to the base. This PCB thus is also part of the chamber wall and the connection is sealed with an O-ring. A more detailed list of the used readout and chip number are in the section about the used readout at 3.4. In figure 3.2, the schematics are shown and in figure 3.3 some pictures of the chamber during assembly and operation.

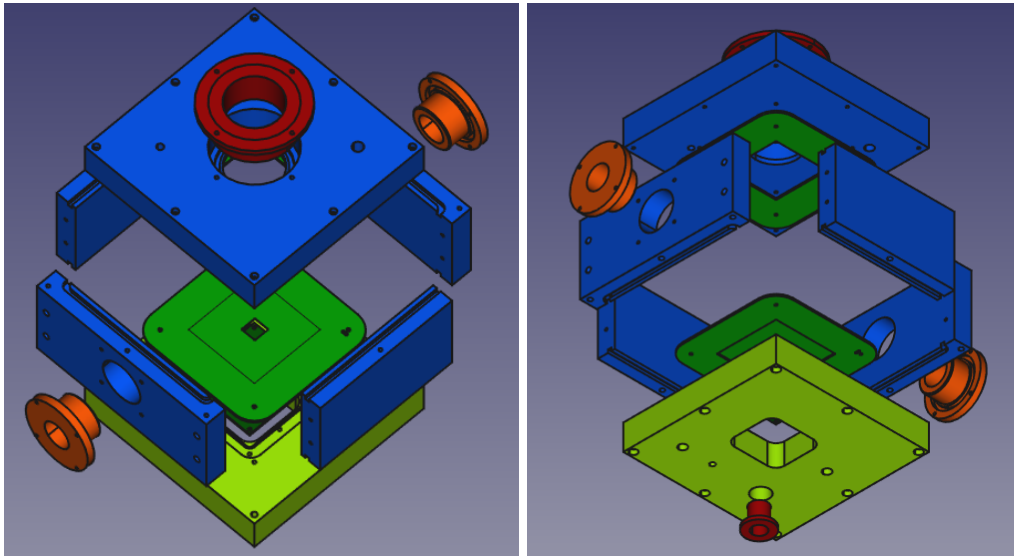


**Fig. 3.2:** Drawing of the chamber main components. Spacers, screws and connectors are not shown. Colour coding: Red, orange: Windows and sensor feed through blue: Chamber walls, light green: Base plate, green: PCB plates for anode and cathode, dark green: Timepix PCB

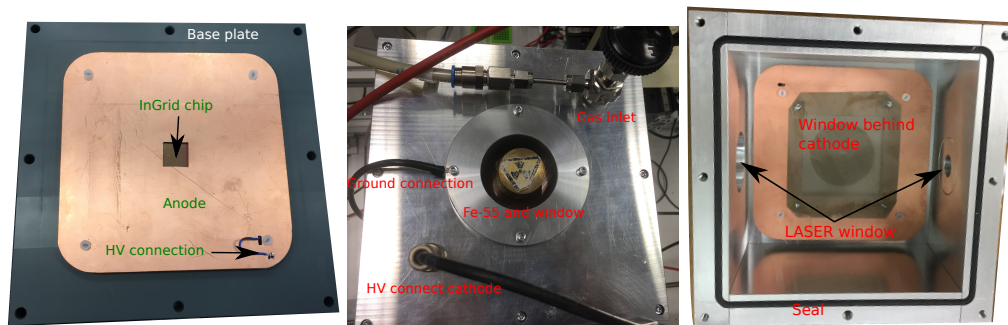


**Fig. 3.3:** Pictures of the chamber during assembly and first tests.

### Electrodes

The electrodes are manufactured from PCB with one sided copper plating. The positions are fixed by M3 screws and polymer spacers to ensure isolation and positioning. Insulation to the chamber walls is ensured by an air gap. The anode has a central cutout for the InGrid, with thinned material in the central region for closer positioning of the chip behind the anode. The cathode has a larger, central cutout, covered in a nickel mesh. The mesh is soldered to the copper plating, ensuring a flat surface. The mesh has a thickness of  $50\ \mu\text{m}$ , a ratio of holes to surface of 0.355 and was manufactured by Stark for screen printing.

#### High voltage supplies

The high voltage supplies are connected to the inside of the chamber by SHV cables and connectors. For gas tight connections, Pasternack PE4500 connectors are used. These connectors are for anode, cathode and the grid of InGrid. They seal by a O-ring and the treads are cut into the plate. For generation of the high voltage, three separate power supplies are used and controlled in manual mode. High voltage is supplied by Iseg NHQ 103M for the anode, 204M for the grid and 208L for the cathode.

#### Radiation windows

For the top window, a Kapton sheet is glued to the insert and the insert is screwed to the lid. This forces the lid on the O-ring to ensure a gas tight seal.

For the smaller windows on the sides of the chamber exist different versions. All versions seal by a O-ring between the rim of the window frame and the chamber wall and are secured by four M3 screws. One set of windows has a additional groove on the outside for an O-ring and treads, enabling the use of acetal inserts with Mylar or sapphire glass windows of an older chamber. The second set have a larger inner diameter, covered with a foil glued to the window.

#### Pressure measurement

The internal pressure and temperature is monitored by a BarometerBricklet v2. This device is using a LPS22HB pressure sensor, capable of measuring temperature and pressure. It has a precision of 1 hPa and 1.5°C

## 3.3 Signal generation

For the generation of test signals inside the chamber, several means exist and the chamber has several ports for this purpose. Since the setup has no veto against external radiation, background radiation and cosmic rays also contribute in the data.

### 3.3.1 UV LASER

The chambers sapphire glass windows can be used to shoot a pulsed UV LASER parallel to the chip surface. The LASER emits at 266 nm by using two stages of second harmonic generation on a beam with 1064 nm. The pulse is triggered by a transistor-transistor logic (TTL) signal supplied by an arbitrary waveform generator.

#### 3.3.2 $\beta$ source

A  $^{90}\text{Sr}$  source with 37 MBq can be used to emit  $\beta$  radiation in the chamber, usually using the side ports. The emissions are caused by two different isotopes. The first decay is  $^{90}\text{Sr} \rightarrow ^{90}\text{Y} + e^- + \bar{\nu}_e$ , followed by a decay of Yttrium  $^{90}\text{Y} \rightarrow ^{90}\text{Zr} + e^- + \bar{\nu}_e$ . The emission of the source is a combination of two different spectra with maximum energies of 0.546 MeV for Sr and 2.28 MeV for Y. The branching ratio into photons is very small for both decays and can be neglected.

#### 3.3.3 X-ray source

The used X-ray source is a  $^{55}\text{Fe}$  source. The isotope undergoes an electron capture, followed by emission of an Auger electron or a photon. Several lines are emitted, in case of photons the emission of the  $K_\alpha$  and  $K_\beta$  lines of Mn are separated by approximately 11 eV and contribute the majority of photons at  $E \approx 5.895$  eV. The branching ratio into these two lines is 25.4%. Additionally, approximately 4% decay into photons of other energies and the remaining branching ratio are Auger electrons. The range of keV electrons in most gases is less than 1 mm. All Auger electrons are absorbed in the source or in the air before entering the sensitive region of the detector, resulting in the test signal containing only photons. During measurement the activity was 40 MBq.

#### 3.3.4 Variable X-ray source

For tests with different photon energies, a variable X-ray source was used. The source is an Amersham AMC.2084 source, with the details available in its data sheet [Amc]. The source contains 37 MBq (10 mCi)  $^{241}\text{Am}$  with a half-life of 432 years almost exclusively via  $\alpha$  decay. The daughter nuclide  $^{237}\text{Np}$  has a half-life of  $2.14 \times 10^6$  years. The decay of americium has a branching ratio of 85% for the emission of the  $\alpha$ , followed by a photon of 59.5 keV and 13% for 103 keV. A series of targets made of different materials can be placed in front of the annular primary source. The photons are then absorbed and excite fluorescence in the target. By the choice of target, the produced energies can be selected. These fluorescence X-rays are collimated into a beam of 0.5 steradian by the hole of the annular primary source and the source casing. The photon rate and energy are strongly dependent on the used target, details can be found in table 3.1. It should be noted that the  $K_\alpha$  line is the stronger line and both lines are actually a combination of different transitions. Ignoring effects of orbitals and coupling between electrons and electrons and the nucleus, the energy for a transition can be calculated using equation 2.2.



Target	$K_\alpha$	$K_\beta$	Rate $\frac{\text{photons}}{\text{sec per steradian}}$
Cu	8.04	8.91	2500
Rb	13.37	14.97	8800
Mo	17.44	19.63	24000
Ag	22.10	24.99	38000
Ba	32.06	36.55	46000
Tb	44.23	50.65	76000

**Tab. 3.1:** Rates and energies for the variable X-ray source, reproduced from data sheet 11196, [Amc]

## 3.4 Readout

The readout uses a Timepix 2 chip with InGrid for amplification and detection of electrons. The data is taken as frames, collecting signal for a defined shutter time. After the shutter is closed, the chip is read out and the data written to storage. The global threshold, THL, suppresses all events below a certain strength. This suppresses most of the noise in the chip. The chip ID of the Timepix chip is 168993, D3 W66. The readout uses an intermediate board v12a and 2m high definition multimedia interface (HDMI) cables for data transfer to the adapter card. The adapter card is connected to a Xilinx Virtex 6 ML 605 FPGA. The version of Timepix Operating Software (TOS) is 8.3.

## 3.5 Expected behaviour

The planned operating conditions are a 80:20 mixture of argon and carbon dioxide at room temperature and pressure. With the planned drift field of  $50 \frac{\text{V}}{\text{mm}}$  it is possible to calculate the expected diffusion during drift and the initial size of the cloud of electrons.

### 3.5.1 Range of photons in gas mixture

It is useful to estimate the range of photons with energy in the region of interest in the gas mixture. Since the intensity of X-rays in matter follows an exponential function, the attenuation length  $\lambda$  is the distance for a reduction to  $\frac{1}{e}$  of the initial flux. Absorption data available from [Ber+10] can be used to estimate the range. Using the available information, energy dependency of the attenuation length is shown in figure 3.4 combining data for argon and carbon dioxide with appropriate scaling. The sharp peak at 3.2 keV is K-edge of argon.

Other absorption lines, for example K lines for carbon or oxygen, are not visible on the chosen scale and would appear below 500 eV.

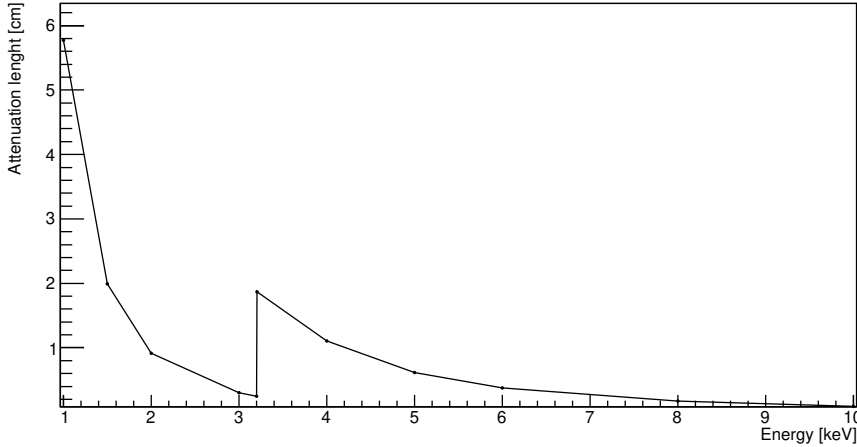


**Fig. 3.4:** Range of photons of different energies in Ar:CO<sub>2</sub> 80:20.

#### 3.5.2 Number of initial electron ion pairs

The mean number of electrons can be calculated with the average energy per ionisation for the gas components, weighted with their concentration. The average energies are  $W_{\text{Ar}} = 26$  eV and  $W_{\text{CO}_2} = 33$  eV, their weighted mean  $W = 27.4$  eV. For the Fe-55 source, the average number of electrons per photon is  $N_{\text{Fe}} = \frac{5.895 \text{ keV}}{27.4 \text{ eV}} = 215$ . This will be a reference value for estimation on the efficiency of the detector and the analysis algorithm.

#### 3.5.3 Effect of $K_\alpha$ and $K_\beta$

The K lines are generated when a hole in the K shell is filled by an electron from a higher shell. This gives rise to a split of the line, with the energy and branching ratio depending on the shell from which the electron filling the K shell originates. Using the branching ratios and energies from [Clo+73], a simulation for this effect is done. The simulation uses the Mersenne twister implementation of TRandom3 in root to simulate  $10^7$  entries. The first step takes a random number in the interval  $[0,1]$  to decide if an entry is simulated with the energy of the  $K_\alpha$  or  $K_\beta$  line. The peak width is chosen based on the data, since the width of the line in the detector is dominated by the energy resolution of the detector. The position of the peak is calculated by the energy calibration of the detector, to estimate the systematic error. Both spectra, as well as their superposition are drawn to compare the peak position and width. The effect is used to estimate a systematic error on the peak position.

The energies and branching ratios for the different X-ray lines are shown in table 3.2.

Target	$E_{K_\alpha}$ [keV]	$E_{K_\beta}$ [keV]	$\frac{BR(K_\alpha)}{BR(K_\beta)}$
Fe	5.90	6.49	7.5
Cu	8.04	8.91	7.4
Rb	13.37	14.97	5.8

**Tab. 3.2:** Energies and branching ratios for the used X-ray lines. Data from [Clo+73] and [Amc]

The resulting spectra are shown in figure 3.5, with the spectrum for both lines, as well as their superposition shown. The spectra are simulated for the initial number of electrons. By taking the relative error instead of the absolute error, the effect of the detector on the observed peak position should be accounted for. With the branching ratios and energies from table 3.2, the expected spectra are simulated with  $10^7$  entries and  $\sigma = 10$ . For the simulation, the initial number of electrons is taken to be  $N_e = \frac{E}{W}$ . The plots are shown in figure 3.5. For the lower energies, the energy difference between the two lines is small and the branching ratio in the  $K_\beta$  line is low, resulting in very little influence on the mean value.

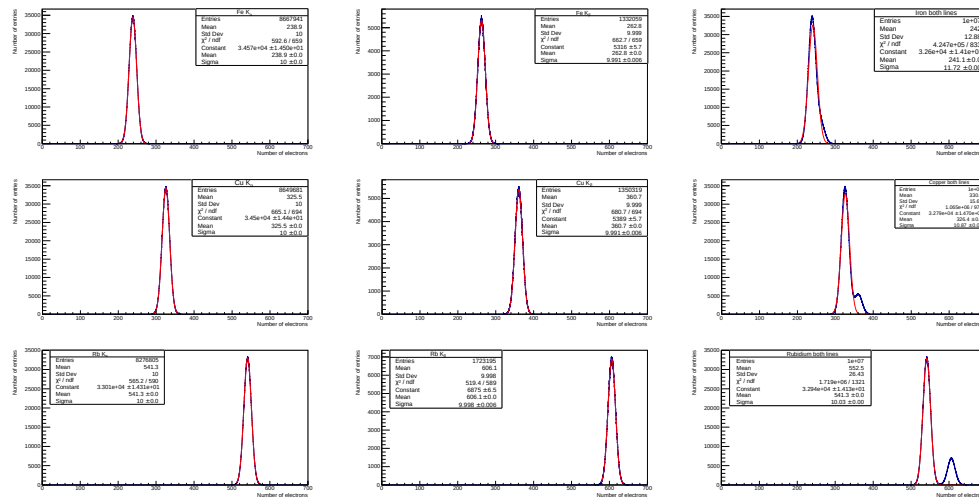


**Fig. 3.5:** Simulated spectra for the K lines of different elements. From left to right:  $K_\alpha$ ,  $K_\beta$  and superposition of both lines. From top to bottom: Iron, copper and rubidium

Since the relative shift is independent of the scale of the x axis and only depends on the energies and branching ratio, only the width of the distribution had to be known from section 5.2. The relative errors are for iron 1.3%, for copper 1.4% and for rubidium 2.1%. This

is calculated from the mean values of the histograms  $\mu$  as  $\sigma_{\text{relative}} = 1 - \frac{\mu_{\alpha}}{\mu_{\alpha\beta}}$ . These results are summarised in table 3.3. While the effect on the peak stays the same, the peaks may merge if the energy scale changes and the width does not. This will not change the shift in the peak position, since the relative positions between the peaks and the zero point do not change.

Source	Peak $K_{\alpha}$	Peak combined	Error
Fe	239	242	0.013
Cu	326	330	0.014
Rb	541	552	0.021

**Tab. 3.3:** Summary of the results for the simulated spectra.

#### 3.5.4 Extension of initial electron cloud

The aim is to calculate an upper bound on the initial size of the electron cloud. Several effects should be taken into account. Since the first step is an energy transfer of a photon to an electron, it is important to know the stopping power of the gas mixture as a function of electron energy. Using energy loss data like [BS82] can be used to approximate the range. For electrons, the approximate range at 5 keV is  $d = 800 \mu\text{m}$ . Since the electron direction parallel to the direction of the photon, most of this distance will appear as a longitudinal extension of the electron cloud.

#### 3.5.5 Size after diffusion

For this parameter, only a maximal size can be estimated. The diffusion constant can be found by Monte Carlo simulations or experimental methods, for example in [AS11]. But the initial distance of the electron cloud generated by the photon is not known and takes any value in the interval  $[0, 5 \text{ cm}]$ . With diffusion constants from [AS11], the diffusion constant for the used mixture and conditions is approximately  $D_T = 150 \frac{\mu\text{m}}{\sqrt{\text{cm}}}$ . Using the maximal drift distance, a Gaussian distribution with a radius of  $\sigma = 340 \mu\text{m}$ , or 6.8 pixel, is expected. It should be noted that the drift parameter has a very strong dependency on field strength. Since the distribution is a two dimensional Gaussian, approximately 40 % of the electrons are expected in a circle with radius  $1 \sigma$ . In case of the Fe source, this would distribute 86 electrons on 145 pixel of the chip. The probability of two electrons in a single pixel is 57 %.

## Data handling and analysis

This chapter describes the design of the software for this analysis. It consists of several different sub units and utilises the Root version 6.16 [Rad+19]. The general analysis strategy has as first step the conversion of the raw txt files into root files. During the analysis, frames are read from the file, hot pixels identified and removed and different algorithms applied to separate signal and background. The signal is then used to reconstruct a energy spectrum. As a convention, the chip is taken to be in the x-y plane and the drift direction is in z direction.

### 4.1 General concept of reconstruction

The electrons created by the X-ray photon diffuse during the drift to readout. This results in a 3 dimensional, Gaussian cloud of electrons. The distribution is symmetric perpendicular to the direction of drift, while parallel to the drift direction the diffusion coefficient is different. Since the data is taken in TOT mode, the different arrival times, caused by the diffusion in z direction, are not visible. As a result, the expected shape of the electron distribution is symmetric in the x-y plane. The width of this distribution will increase, as described by equation 2.9. If the drift distance is sufficiently large, almost all electrons are separated by more than one pixel, while still spaced close enough to identify all electrons generated by the initial photon. The goal is to find all hit pixels that belong to one initial photon and to reject background events and noise of the chip. The number of electrons, combined with the average energy per ionisation for the gas mixture, can then be used to calculate the photon energy, assuming the efficiency for the detection is known. The chosen approach is to identify and remove noisy and damaged pixels first and setting their value to zero, followed by a sequential recombination algorithm. An overview of these algorithms can be found in [CSS08], while the implementation in this analysis is described in 4.3.2. The

reconstruction generates a set of containers, one for each reconstructed cluster, containing all available information on the pixels contained in the cluster. This enables easy calculation of further parameters of the clusters and fitting functions.

### 4.2 Reader

The reader function generates the full file name based on the frame number and is able to handle both full matrix and zero suppressed data. It generates the Root name tag based on the frame number, while the title contains the full information including timestamp for each frame to enable identification and extraction of additional information like timing. It is possible to save the data as root histograms or root tree data. There is no change in the pixel data at this stage beyond a conversion of format. This enables faster access and a compression of by more than one order of magnitude in size and the merging of several thousand individual text files into one file for easy handling.

### 4.3 Analysis package

The analysis package is designed to accept the data after conversion by the reader package. It identifies the frames by their frame number and applies several functions for data preparation. These are described in the following subsections. A visualisation of the steps in the program is shown in figure 4.1. The different steps are explained in more detail in the next parts.

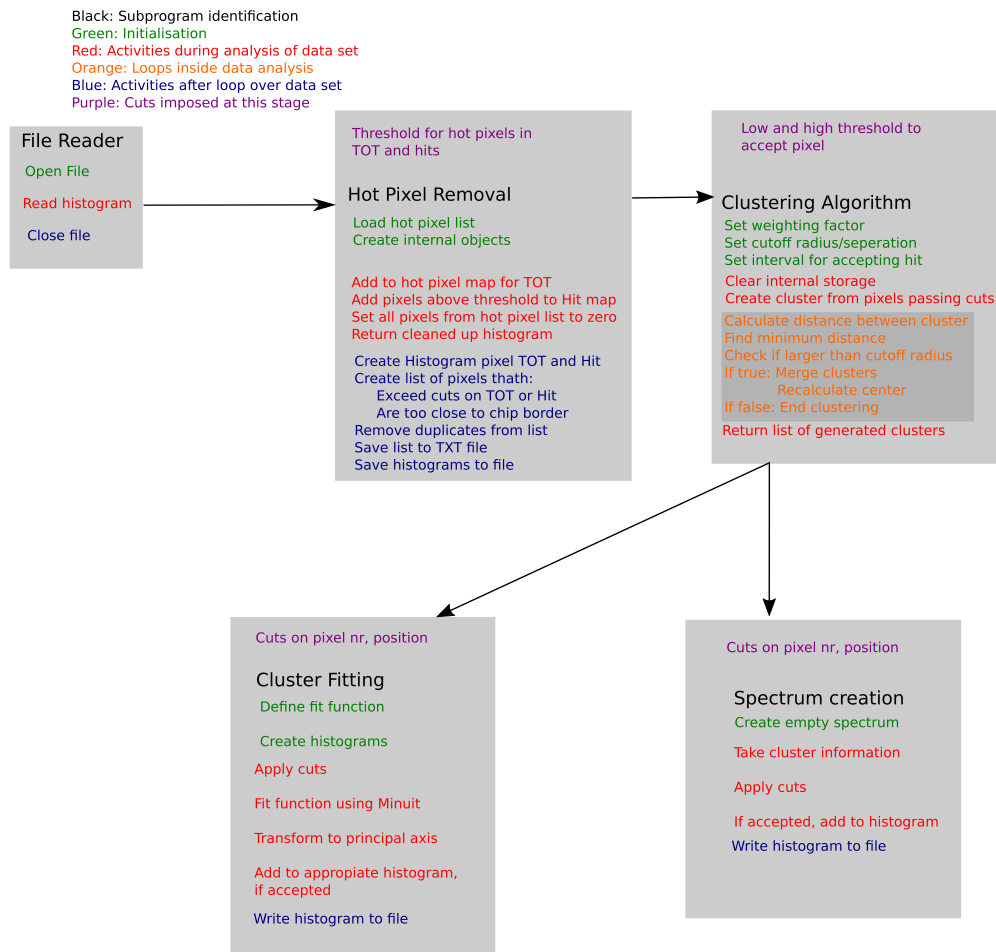


Fig. 4.1: Program flow of analysis package.

#### 4.3.1 Hot pixel identification and removal

The response of different pixels of the Timepix chip is homogenised by the threshold equalisation matrix, generated by the calibration functions of TOS. Some pixels may show a bad behaviour, in most cases a high TOT value in absence of signal. These pixels, referred to as “hot pixels”, should be disregarded and removed. The package for hot pixel removal contains two major parts. The first is responsible for the identification of hot pixels and generates a list of all hot pixels in the process explained in 4.3.1. The second part uses this list to set these pixels to zero.

### Identification of hot pixels

The package has a `AssignHistogram` function, this function copies all pixels of the histogram and adds them to a 2D histogram called “hot pixel mapTOT”. This histogram contains the total sum of clock cycles a pixel was active. This information is only meaningful for TOT data. For the use of TOA mode and as an additional tool to identify hot pixels in TOT mode, a second histogram “hot pixel mapHit” contains the information how often each pixel exceeded a user defined threshold, usually set to 1. The method for identification of hot pixels proceeds in the same way. In this thesis, both cuts are used simultaneously. After the reading in of data is complete, a 1D histogram containing the 65536 entries of the map histogram is generated. On the x axis the number of hits or clock cycles is plotted, while on the y axis the number of pixels is plotted. This histogram enables the user to choose the position of a cut. The cut above which a pixel is flagged as hot may either be an absolute value or relative to the highest value of all pixels. An example for the 1D histogram used to determine the position of the cut is shown in figure 4.2, in this case for TOT mode.

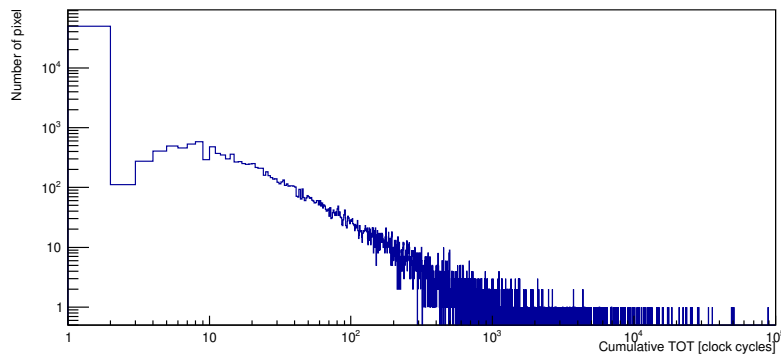


**Fig. 4.2:** Example of a distribution for determination of the hot pixel cut, in TOT mode. Data from run 258, with the cut indicated by a red line.

In this example, the cut would be chosen at 750 clock cycle, removing a few hundred pixel. The same can be done for hits.

### Creation of the hot pixel list

After the cut for the hot pixels has been chosen, a function “`FindHotPixels`” searches for all pixels exceeding the set threshold for hot pixels in both hit and TOT maps. If a pixel exceeds the cut, its x and y position is added to a list of hot pixels. In addition, a “`RemoveBorders`” function adds the pixels within the chosen distance from the border of the chip to the list of



hot pixels. These functions can be used to remove data from areas of the chip by hand. After all pixels to be removed have been added to the list, the function “CleanupList” removes all duplicated entries. “WriteList” writes this hot pixel information into a text file.

### Removal of hot pixels

In order to remove hot pixels, the list of hot pixels is loaded. Every histogram passed into the function “RemoveHotPixels” has the pixels from the hot pixel list set to zero. For this reason it is also important to first assign a histogram to “FindHotPixels” before “RemoveHotPixels”.

### 4.3.2 Creation of clusters from pixel hits

In the next step, an algorithm is used to reconstruct the primary ionisation from the signal on the Timepix chip. The first step is converting each pixel to an entry in the cluster list. These entries contain several information, including the coordinates and TOT of each pixel merged into them. Other information saved are the position of the center and for the use in TOT mode the total clock cycles of the cluster. These initially created proto clusters are then merged in an algorithm. In figure 4.3 two frames from a data set are shown. The shape of clusters is visible, thus motivating the use of a jet algorithm.

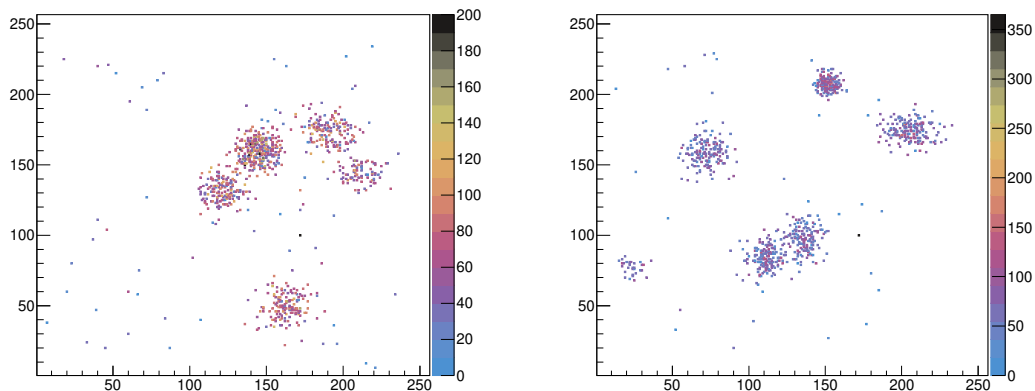


**Fig. 4.3:** Example of frames from a data set taken using InGrid and X-ray photons.

### Sequential combination of clusters

The algorithm used is an implementation of the Cambridge Aachen algorithm usually used in high energy physics to reconstruct jets. By changing the weighting factor for clock cycles it is also possible to use the kT and anti-kT algorithm. This only changes the measure for

calculating the distance between clusters. The general form of the metric is given in equation 4.1

$$d_{ij} = \min(z_i^n, z_j^n) \left( (x_i - x_j)^2 + (y_i - y_j)^2 \right) \quad (4.1)$$

The algorithm differs slightly from the regular jet algorithms, since the distance measure is usually divided by  $R^2$  and calculated in detector coordinates. These are similar to cylinder coordinates, using pseudo rapidity, azimuth angle and transverse momentum. For the distance for a flat detector it is convenient to use cartesian coordinates for the distance, with the TOT taking the role of the momentum.

The used algorithm also has a different criterion to identify the completion of clustering. The used criterion is, that the distance between the two closest clusters has to exceed a set value  $R$ . Since  $n = 0$  is used in this thesis, this is just the distance between the center of gravity of both clusters. This differs from the algorithm for jets, as there is no additional criterion to remove clusters close to the beam axis.

### 4.3.3 Fitting of Gaussian and ellipse

The final step is the fitting of a Gaussian using the Minuit package of root. Since we only distinguish between hit and no hit, all pixels that belong to the cluster are set to 1. It is important to note that the fit only contains the pixels that have been assigned to the cluster, all other pixels are assumed to be zero during the fit. The Gaussian has a total of six parameters. The first two are  $\mu_x$  and  $\mu_y$ . They give the position of the mean in x and y direction. The next two are the variance in x and y direction,  $\sigma_x$  and  $\sigma_y$ . In addition, it has a correlation coefficient  $r$  between x and y, as well as a normalisation constant  $N$ . The definition of the function is chosen in such a way, that the constant  $N$  is the number of entries. The definitions for the Gaussian and the covariance matrix follow [Shi18].

$$f(x, y) = \frac{N}{2\pi\sigma_x\sigma_y\sqrt{1-r^2}} \exp\left(-\frac{\frac{(x-\mu_x)^2}{\sigma_x^2} + \frac{(y-\mu_y)^2}{\sigma_y^2} - \frac{2r(x-\mu_x)(y-\mu_y)}{\sigma_x\sigma_y}}{2(1-r^2)}\right) \quad (4.2)$$

If the coordinate system has an angle of  $\frac{n\pi}{2}$  with respect to the principal axis of the contour ellipses of the Gaussian, the correlation matrix is in diagonal form. The correlation matrix is shown in equation 4.3.

$$M = \begin{pmatrix} \sigma_x^2 & r\sigma_x\sigma_y \\ r\sigma_x\sigma_y & \sigma_y^2 \end{pmatrix} \quad (4.3)$$

Calculation of the eigenvalues is straight forward and the result is shown in equation 4.4. Only the positive square roots of  $\lambda$  are taken into account.

$$\lambda_{1,2} = \frac{\sigma_x^2 + \sigma_y^2}{2} \pm \sqrt{\frac{(\sigma_x^2 + \sigma_y^2)^2}{4} - \sigma_x^2\sigma_y^2(1-r^2)} \quad (4.4)$$

The last missing parameter is the angle between the coordinate system generated by the principal axis and the xy coordinate system. Using 2x2 rotation matrices, a relation between the off diagonal matrix elements of M and the angle can be found. This is done by rotating the diagonal form of the matrix. The off diagonal element of the rotated matrix can be identified with the off diagonal element of M. The rotation is shown in equation 4.5, with  $\lambda_{1,2}$  denoting the square of the principal axis.

$$\begin{aligned} & \begin{pmatrix} \cos(\alpha) & -\sin(\alpha) \\ \sin(\alpha) & \cos(\alpha) \end{pmatrix} \begin{pmatrix} \lambda_1 & 0 \\ 0 & \lambda_2 \end{pmatrix} \begin{pmatrix} \cos(\alpha) & \sin(\alpha) \\ -\sin(\alpha) & \cos(\alpha) \end{pmatrix} \\ &= \begin{pmatrix} \lambda_1 \cos^2(\alpha) + \lambda_2 \sin^2(\alpha) & (\lambda_1 - \lambda_2) \sin(\alpha) \cos(\alpha) \\ (\lambda_1 - \lambda_2) \sin(\alpha) \cos(\alpha) & \lambda_1 \sin^2(\alpha) + \lambda_2 \cos^2(\alpha) \end{pmatrix} = \begin{pmatrix} \sigma_x^2 & r\sigma_x\sigma_y \\ r\sigma_x\sigma_y & \sigma_y^2 \end{pmatrix} \end{aligned} \quad (4.5)$$

The resulting equation 4.6 can be solved for  $\alpha$  by using  $\sin(2\alpha) = 2\sin(\alpha)\cos(\alpha)$ . The resulting equation can be used to extract the angle  $\alpha$ .

$$r\sigma_x\sigma_y = \sin(\alpha)\cos(\alpha)(a^2 - b^2) \Leftrightarrow \sin(2\alpha) = 2\frac{r\sigma_x\sigma_y}{b^2 - a^2} \quad (4.6)$$

The eccentricity of an ellipse is defined by equation 4.7.

$$\epsilon = \sqrt{1 - \frac{b^2}{a^2}} \quad (4.7)$$

#### 4.3.4 Creation of energy spectrum

Two different types of spectrum may be created. They are labeled as ‘‘Hit’’ and ‘‘TOT’’. TOT actually contains the number of clock cycles the pixels have been above threshold, while Hit only counts how many pixels passed the TOT cuts of the clustering algorithm. Clusters assigned to these spectra can be subjected to different cuts to reduce the contributions of background and noise.

##### Cluster discrimination

Several cuts are usually imposed on the data. The first and most basic is the removal of the identified hot pixels at the beginning of the analysis process. This aims to reduce the noise of the chip, but since noise is mostly homogeneous on the chip this would introduce just a shift to higher values for the peaks. In case of algorithms with a weighting factor like  $k_T$  and anti- $k_T$  this could disrupt the clustering by introducing pixel with high weight but no correlation to the signal.

At the beginning of the clustering, two cuts are introduced on the ‘‘TOT’’ value of the individual pixel. They require the pixel value to be in the interval  $[\text{Cut}_{\text{low}}, \text{Cut}_{\text{high}}]$  to be added

to the list of proto clusters. This is to remove low “TOT” entries, caused by the normal noise of the chip.

After clustering the center of each cluster is known. At this point a cut is imposed to remove clusters in the border region of the chip from the analysis. Clusters close to the chip border are likely affected by distortions in the electric field and may be split between anode and readout. The field distortions may change the shape of a cluster, deforming it in a direction perpendicular to the chip border. A splitting between the InGrid readout and the anode will cause the cluster to lose entries, an effect that is further enhanced since the borders of an InGrid chip have no grid for charge multiplication. This would cause a systematic error by shifting the TOT and number of entries for a reconstructed cluster to smaller values. By rejecting clusters that may be affected, this effect can be avoided.

### **Readout speed monitor**

A small package reads out the timestamp of the frames and generates a distribution of the time interval between two frames, which is the sum of shutter window and the time for readout and storing of the frame. This is done to monitor the readout speed of the chip.

### **4.3.5 Additional software**

Several, simple programs are used for purposes like to monitor the properties of the gas.

#### **Gas monitor software**

The gas monitor is read out by a MCA and the results are stored as text files. This is controlled by a macro file for the MCA. A simple script reads these files and searches for the full absorption peak in the spectrum. The peak position is in these graphs shown on the y axis in arbitrary units, while the timestamp is shown on the x axis, scaled in minutes. This is used to observe the time needed to establish a stable gas mixture inside the chamber and verify stable amplification. The peak position is given in arbitrary units.

## Measurements and results

The experimental results can be split into several parts. The first part is the commissioning of the chamber. The second part are measurements with a 40 MBq Fe-55 source and adjustment of operating parameters. The third part is done with additional photon energies of the variable X-ray source. Raw frames, data as it was taken by the chip, are converted to histograms for handling and visualisation purposes, and contain hot pixels. A “Hit” is every pixel that is active for more than one clock cycle.

### 5.1 Commissioning stage

After the assembly is completed using a defective chip without grid, tests to ensure safe operation at the planned voltages are done. The chamber was filled with the gas mixture and the outlet closed to increase internal pressure and thus leak rates. A gas detector is then used to search for gas leakage. During this test, no excessive leakage was detected. Some minor imperfections of the rubber seals at the radiation windows were corrected after the test and showed a decreased leakage afterwards. In the next step, the outlet was opened and the voltage on the cathode was increased to the expected maximum operating voltage of 3500V. Between 3450 V and 3500 V a discharge between cathode and chamber was observed and the test stopped. This problem was solved by adding a Kapton tape to cover the cathode edges and the edges of the nickel mesh.

During these tests, the gas monitor was used to determine the time until stable conditions inside the chamber were reached. These are usually reached in less than two hours, as shown in figure 5.1. Later results for the gas monitor data are comparable and all show a constant peak position after flushing, indicating stable amplification inside the gas mixture.

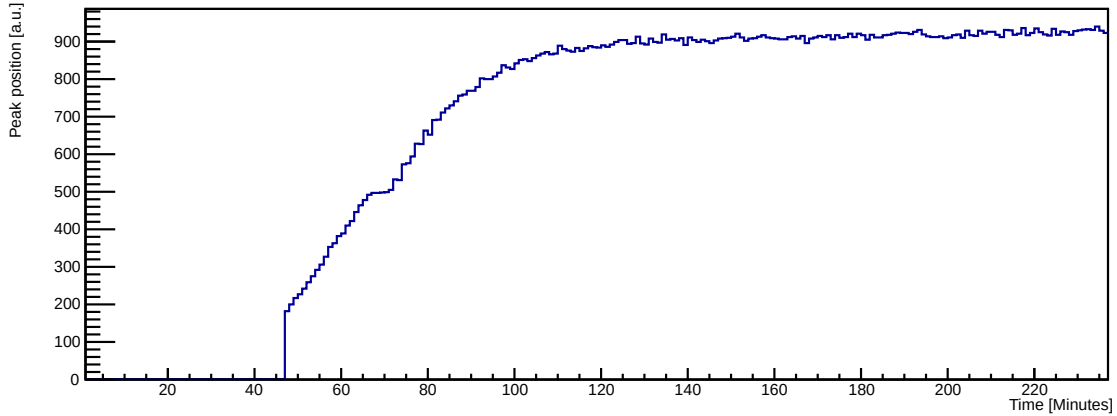


**Fig. 5.1:** Peak position in the gas monitor during flushing. Gas was supplied at the 0 mark.

## 5.2 First test using Fe-55

Before the start of any measurement, an automatic calibration of the timepix chip was done by TOS. The next step was a short phase of data taking to confirm chip function and chamber operation. The first measurements are done using the Fe-55 source to achieve high rates and easy detection of the presence of signal. Operating parameters of the chamber are shown in table 5.1. The shutter time was set to 10 ms and the chip THL to 364.

Field	Distance [mm]	Voltage drop [V]	Field strength [V/mm]
Drift field	64	2935	46
Transfer field	1.2	55	46

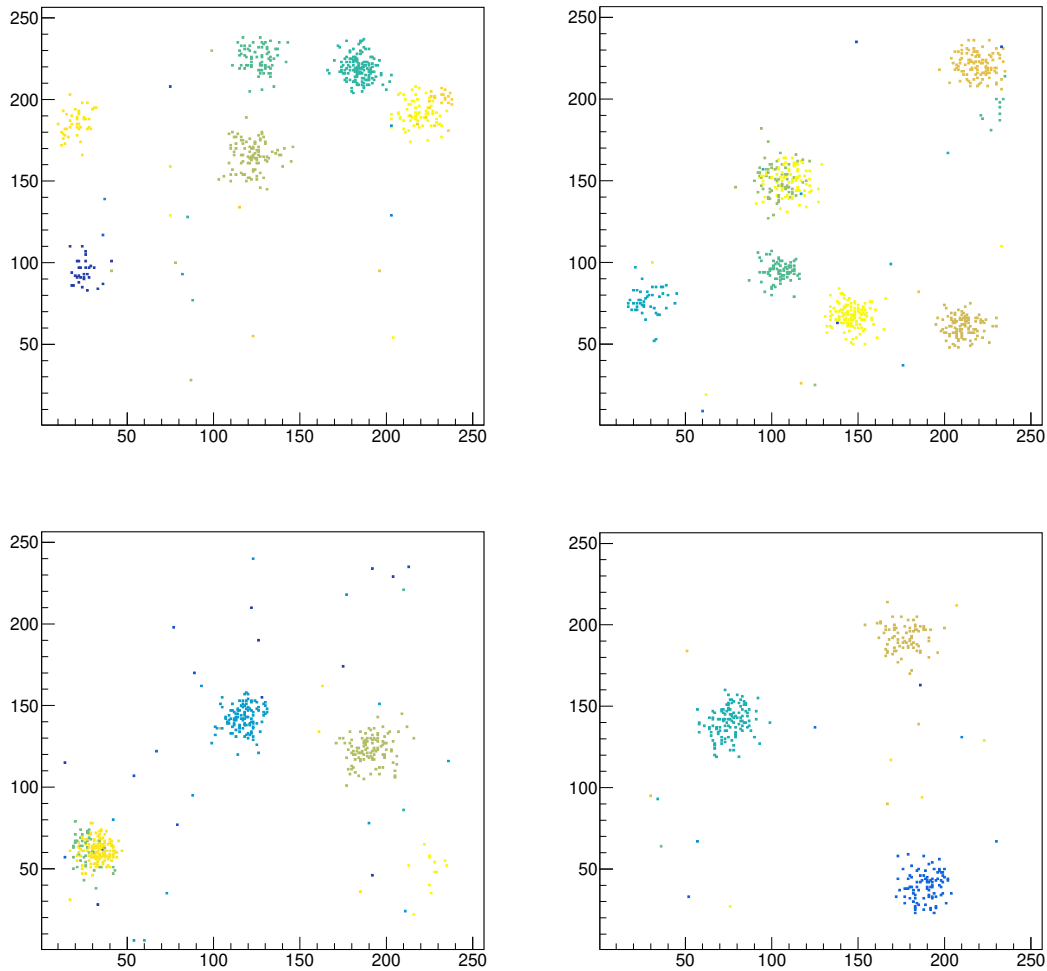
  

Component	Voltage[V]	Distance from Chip [mm]
Timepix chip	0	0
Grid	410	0.05
Anode	465	1.2
Cathode	3400	65
Chamber window	0	70

**Tab. 5.1:** Default parameters of chamber. The distances are the same in every test, while changes in operating voltages are specifically noted.

These tests showed the detection of several photons in one frame, with individual clusters visible by their clock cycle because of the usage of TOA mode. Some of these frames are shown in figure 5.2. This also confirms the assumption of closely spaced hits by X-ray photons in the used drift fields and distances. Individual clusters are clearly visible and can be

distinguished by their TOA values, shown on the z axis.



**Fig. 5.2:** Some frames of the first test run 256. 10 ms shutter window with Fe-55 and THL 364. Chamber fields as in table 5.1. Hot pixels already have been removed.

The test for the time per frame is shown in figure 5.3 and shows, that most time is spend on readout and saving of the data. It is generated from the timestamps of the frames, generated during saving by TOS.

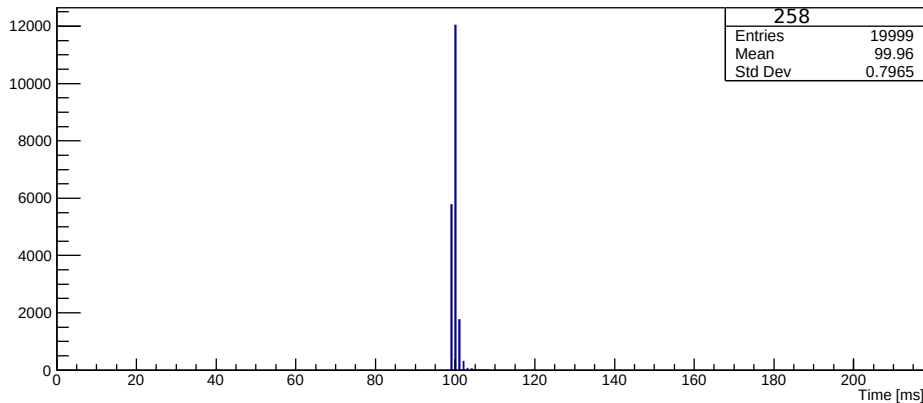


**Fig. 5.3:** Distribution of time between two frames for 10 ms shutter time, taken during run 258.

### 5.2.1 Second test

The second test consisted of three different data sets to confirm operation and investigate the behaviour of the chip and chamber with 20000 frames each. The data is taken at the parameters in table 5.1 with THL at 364 and 880  $\mu$ s shutter time. The first data set is taken during the filling phase and without radioactive source or high voltage, identified as Run 258. It contains only chip noise. The next data set is taken with both high voltage and the Fe-55 source and is labeled Run 259. This data set should contain chip noise, background and signal. A last data set, run 260, for this test was taken with high voltage but the source was removed. This is done to look at the background and chip noise.

### Generation of hot pixel maps

The pixel activity in the data set of Run 258 is shown on the left side in figure 5.4. The distribution is mostly homogeneous and shows little activity in most pixels. If the number of hits in a pixel is plotted as a histogram for the whole chip, the resulting histogram can be used to choose the position of the cut to identify most hot pixels. This plot is shown on the right side, including the chosen cuts at 750 clock cycles and 100 hits. The cut at the borders was chosen as six pixels from the borders of the chip. This cut has little effect on the detection of photons, since the grid does not extend to the chip borders. In total, approximately 300 pixels are removed as hot pixels, together with the cut on the borders this amounts to about 6300 pixels or less than 10%. Since these hot pixels are specific for the used chip, this identification procedure would have to be repeated if a new chip is used. It should be noted that the number of pixel in the list is less than the sum of hot pixels and



the borders, since pixel may appear in both but are only counted once.

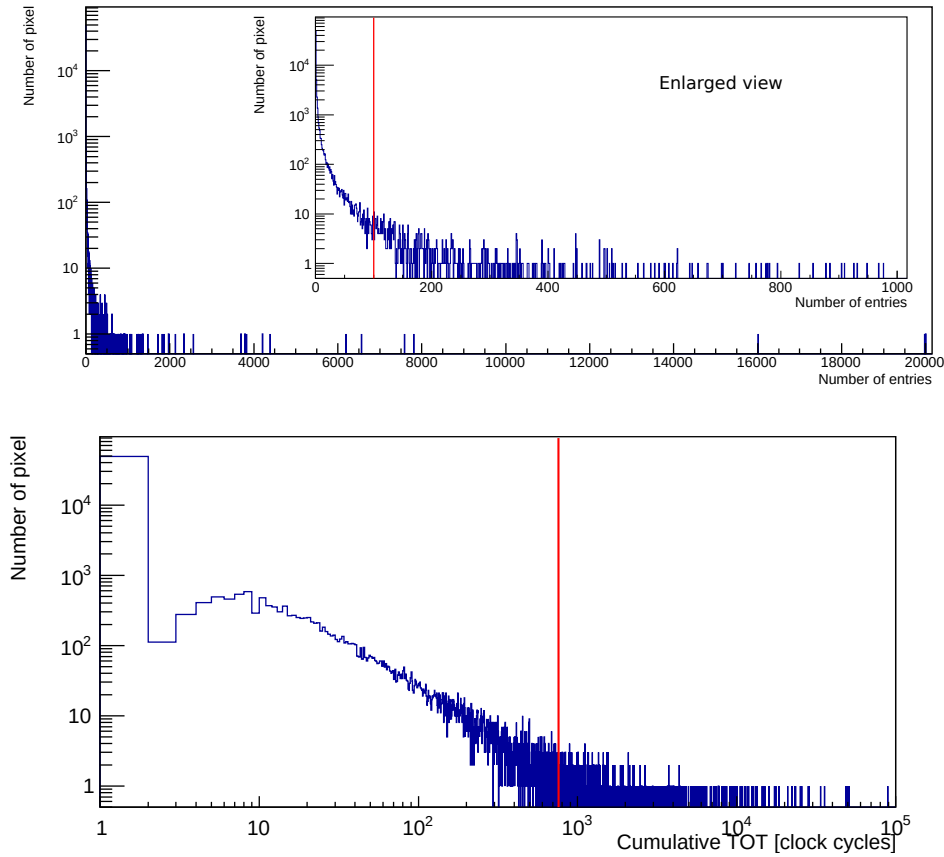


**Fig. 5.4:** Distribution of the hits on the chip during Run 258. A hit is counted if the pixel was active for more than 1 clock cycle. The lower histogram is the histogram for the cumulative clock cycles. The position of the cut on hot pixels is indicated by the red line.

A second test, run 259, in TOT mode showed an increase in signal rate despite a shortened shutter time, reduced from 10000  $\mu\text{s}$  to 880  $\mu\text{s}$ . This was most likely caused by a different placement of the radioactive source. Some frames are shown in figure 5.5. To solve this, a source holder was produced to ensure consistent placement within 0.5 mm in the subsequent tests.

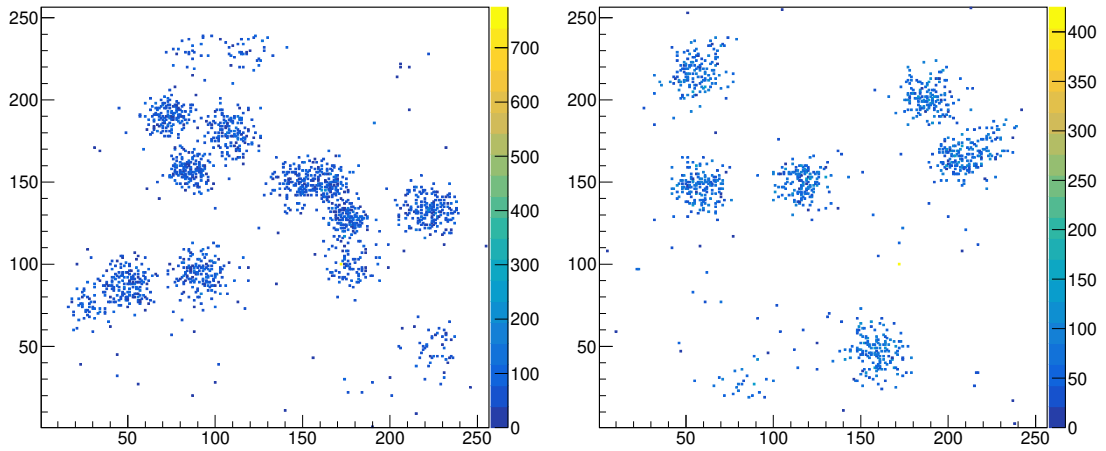


**Fig. 5.5:** Some frames of the second test run 259 in TOT mode. Chamber fields as in table 5.1.

As for the shutter window time of 10 ms several clusters from photons are observed, the shutter time for subsequent tests was reduced to  $880 \mu\text{s}$ .

### Pixel activity for noise, background and signal

This data, in combination with the data set with the high voltage and signal, can be used to see the difference between active pixels caused by chip noise and the avalanche in the amplification gap caused by electrons. For this, a histogram is generated with every active pixel of every frame generating an entry for its TOT value. This is done to create a distribution of the TOT values for the data set, both before and after the removal of hot pixel. Since both signal and background generate free electrons in the gas, it is expected to see a combination of chip noise and a component caused by the amplification and detection of single electrons in the data for Run 259 and Run 260. The hot pixel are already removed at this stage. These histograms are shown for the three data sets in figure 5.6, 5.7 and 5.8. It is visible that hot pixel contribution is significant for TOT values above 200 clock cycles. After removal of hot pixels, the distribution for run 258 shows a behaviour that is characteristic for many amplifier, with an exponential rise for small signal amplitudes. The effect of high voltage, resulting in detection of background events, can be seen between run 258 and 260 as an increase in entries above approximately 50 clock cycles. Additional presence of the iron source in run 259 increases the amount of events further, without changing the shape of the histogram. This effect is also visible in the number of entries and the mean value in the histogram, progressing to higher values.

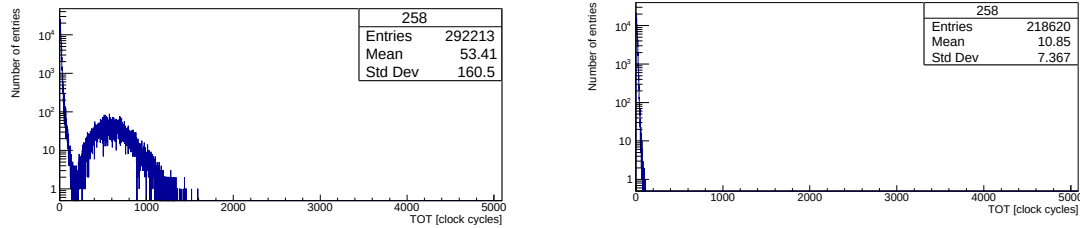


Fig. 5.6: TOT distribution for individual pixels activations for all frames of run 258. Left column including hot pixel, right column after hot pixel removal.

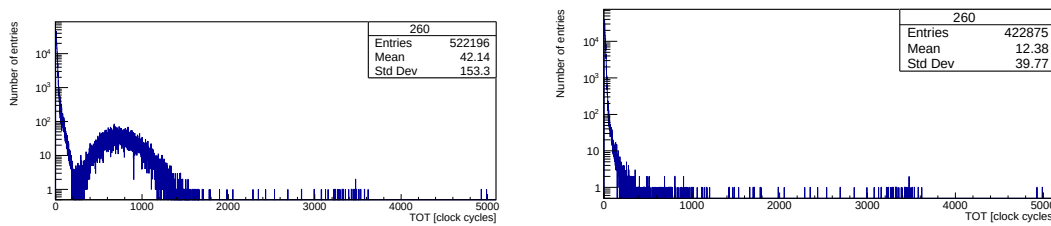


Fig. 5.7: TOT distribution for individual pixels activations for all frames of run 260. Left column including hot pixel, right column after hot pixel removal.

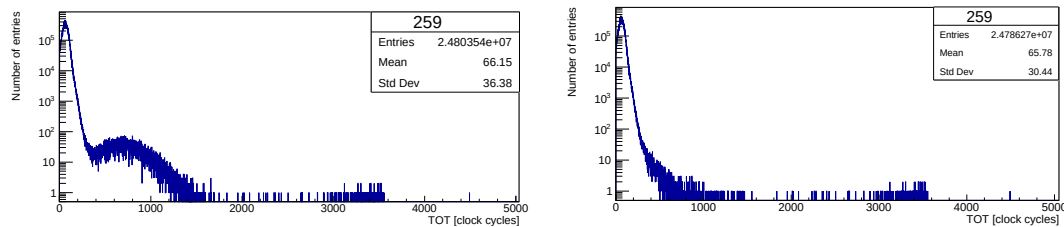
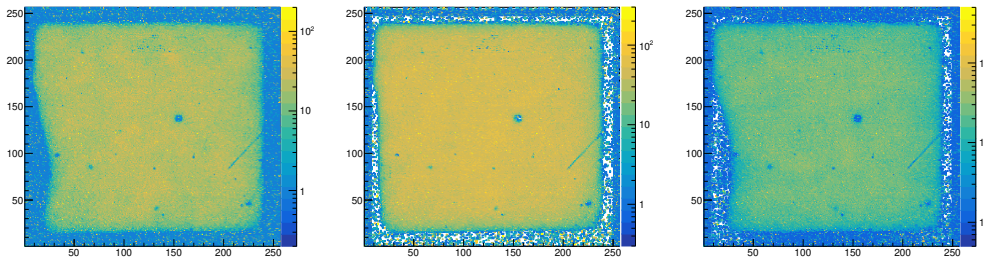


Fig. 5.8: TOT distribution for individual pixels activations for all frames of run 259. Left column including hot pixel, right column after hot pixel removal.

### 5.2.2 Variation of operation parameters

For the next tests the operation parameters of the chamber were changed. Only one parameter is changed, while all other voltages are adjusted to keep field strengths constant. The first step is just a visual check of the occupancy map for effects of a different grid voltage. The normal operating voltage of 410 V in run 263 is increased by 10 V in run 269 and decreased by 10 V in run 266. Voltages higher than 420 V are not tested to avoid discharges and damage to the chip. The occupancy map for hits is shown in figure 5.9, with all data sets taken at 364 THL and 300  $\mu$ s shutter time. The other voltages are changed accordingly

to keep all other field strengths constant.



**Fig. 5.9:** Variation of grid voltage: left run 266, middle run 263, right run 269.

The occupancy maps show a mostly homogeneous inner region and a transition into a region with distortions at the borders. These regions extend approximately 20 to 30 pixels from the chip boundaries and have probably three reasons. The first is the fact that the grid does not cover the whole chip, leading to a region of approximately 10 pixels without amplification. The second effect are field distortions in the drift field and manufacturing imperfections. There is a minor deviation on the corner of the anode facing the connection point for high voltage, matching the rough shape of the anomaly. A third effect is a misalignment of chip and anode in the order of 0,1 mm by the fit of screws and holes in the anode. In data analysis this can be addressed by a cut to remove clusters that extend into these regions. In the following parts, the clustering algorithm is used for reconstruction with radius 25 pixels and requiring 25 clock cycles TOT value for accepting a pixel. The spectrum of the number of entries in the cluster is created to compare to the expected number of entries from full absorption of the X-ray photons. It is also interesting to look at the different peak positions in this analysis when operating voltage of the InGrid is changed. Since the gas amplification depends on the field strength, a comparison of the different operating voltages for the grid and the peak position is shown in figure 5.10. It can be easily verified that the peak position for 410 V and 420 V grid voltage agree within two standard deviations, while the width of the peak increases by approximately 10 %. Since there is no increase in sensitivity, but the risk of sparks and possible damage to the chip is increased at higher operating voltage for the grid, 410 V is chosen for all further tests. Lower operating voltages for the grid reduce the gas amplification and reduce the sensitivity to electrons, causing the peak to shift to a lower number of pixels inside the cluster.

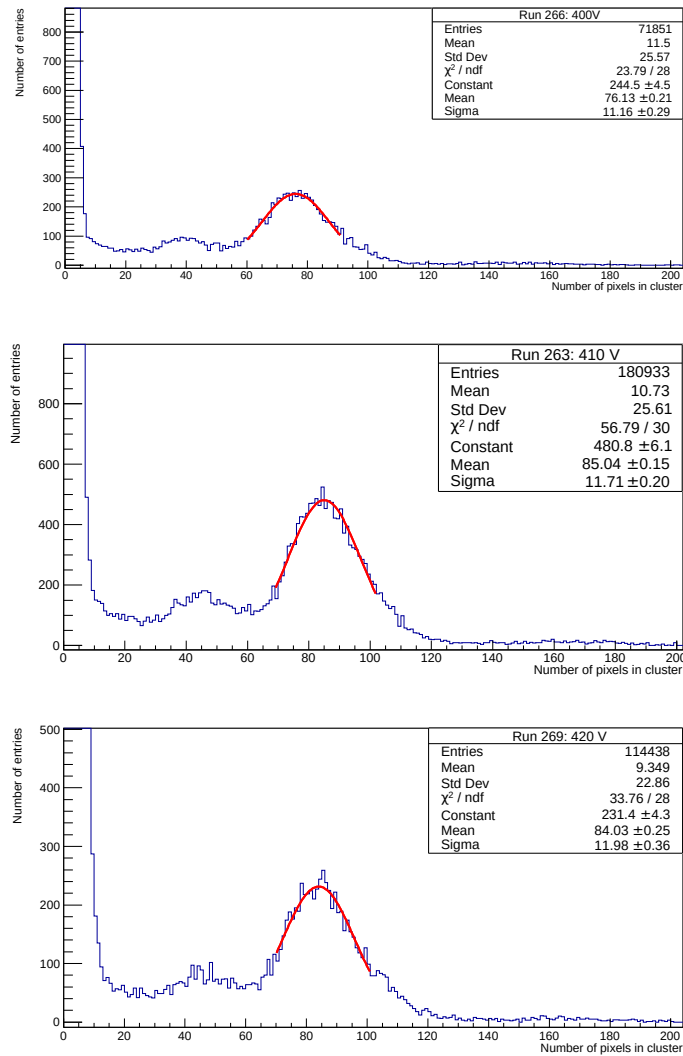
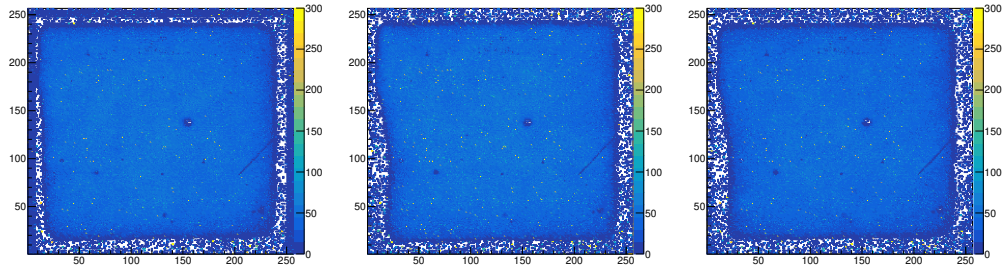


Fig. 5.10: Spectrum variation depending on grid voltage.

It is expected that the border regions show some dependence on the transfer field, which is investigated by changing the voltage for the transfer field by 10 V from its default value of 55 V. The default voltage is used in run 263, while the voltage is increased in run 272 and decreased in run 273. The operating parameters for the chip in this test are 410 V and a THL of 364. The resulting occupancy is shown in figure 5.11. The lowest distortions seem to appear at 55 V transfer field, in which case the field strength between anode and cathode is the same as between anode and grid.



**Fig. 5.11:** Occupancy maps for the variation of the transfer field. From left to right: Run 263, Run 272 and 273.

### 5.2.3 Cluster reconstruction at different stages

To show the effect of the reconstruction algorithm, a single frame of run 287 is shown at different stages. This is to illustrate the look of a raw data frame and the frame without the hot pixels, as well as how pixels are assigned to clusters based on proximity. It should be noted that run 287 has a different shutter time, compared to the previous runs. The progression in figure 5.12 of a single frame during the program. The first frame shows raw data, including hot pixel. The presence of hot pixel increases the z scale to high values, like expected from the distributions in figure 5.7. After removal of hot pixels, the scale is much lower, with a much lower maximum TOT value, likely caused by pile up. The next step is shown after the recursive recombination is completed and each cluster is drawn in a different colour to make the result move visible. At this stage, all cluster with less than 10 entries are suppressed. The last step is a visualisation of the number of pixel contained in the cluster on the z axis. For better visibility, the bin size is increased by a factor of 8.

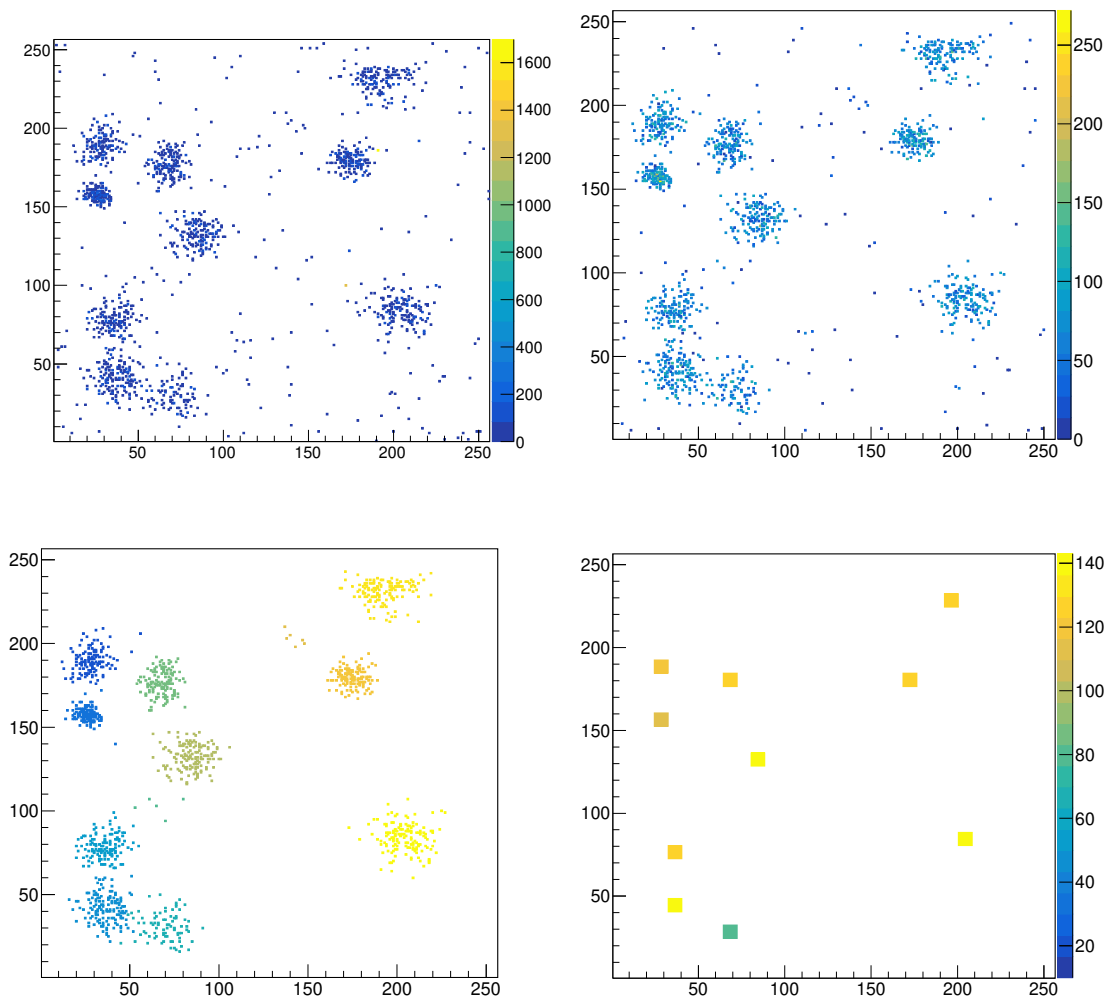


**Fig. 5.12:** Run 287 frame 2 at different stages of analysis. From left to right: First row: Raw data, hot pixels removed. Second row: Pixel belonging to the same cluster in the same colour, number of pixels in each cluster and larger cells for visibility.

### 5.3 Results for different X-ray sources

The measurements have been done with different X-ray energies. It is important to note that the rates for these different sources are quite different and span at least 4 orders of magnitude between the Fe-55 and the variable X-ray source with copper target. Since the Timepix 2 chip and its readout chain is unable to be read out continuously and the setup is not capable of triggering on photons, a set number of frames is taken and analysed. The

low rates make a change in shutter time necessary, resulting in an increase in electronic noise in the chip. The rate of the Fe-55 source is attenuated using absorbers made of paper. This is used to adjust the rate and avoid excessive pile up. All data sets are taken at default voltage settings, as in table 5.1, and 3 ms shutter time and 364 THL. The run number, used source and number of frames in the data set is shown in table 5.2. The radius for the clustering algorithm is set to 25 pixels and pixel have to exceed 25 clock cycles TOT value to be accepted. A hard cut requires the frame to have between 30 and 2500 pixel with a TOT above one clock cycle. The analysis is later repeated with different cuts to investigate its influence on the energy calibration and resolution.

It should be noted that only the  $K_\alpha$  lines are taken into account. This is because the ratio for  $5.6 \leq \frac{K_\alpha}{K_\beta} \leq 7.4$  for the used elements [Clo+73], resulting in a branching ratio between 10 % and 18 %.

Run	Source	Frames
279	Cu	10000
283	Rb	20000
285	Mo	10000
287	Fe-55	10000

**Tab. 5.2:** Run number, source and number of frames for the used data sets.

### 5.3.1 First energy calibration

In the first analysis, the acceptance cut for pixel to count as hit was set to 25 clock cycles. The radius for the cluster algorithm was set to 25 and all clusters are accepted for the spectrum, regardless of position. The peak for full absorption and, if possible, the escape peak are fitted using a Gaussian distribution. Then a plot of the energy of the peak and its position is created. In figure 5.13, these spectra including the fit are shown for each data set. The reducing detection probability for higher energy, as expected by the absorption length, is directly observable in the height of the full absorption peak. This is especially prominent considering the lower number of entries in the peak for rubidium compared to copper, despite a factor of two larger data set. Using the known energy of the X-ray sources and the mean of the Gaussian fit, an energy calibration can be done. The resulting energy calibration is shown in figure 5.14. The spectrum of molybdenum could not be fitted, while the escape peak for the iron source could be used. The available data shows a linear behaviour with photon energy. The errors are calculated from the error introduced by the presence of the  $K_\beta$  line  $\sigma_K$  and the error of the Gaussian fit  $\sigma_{\text{fit}}$  as  $\sigma = \sqrt{\sigma_{\text{fit}}^2 + \sigma_K^2}$ .



### 5.3 Results for different X-ray sources

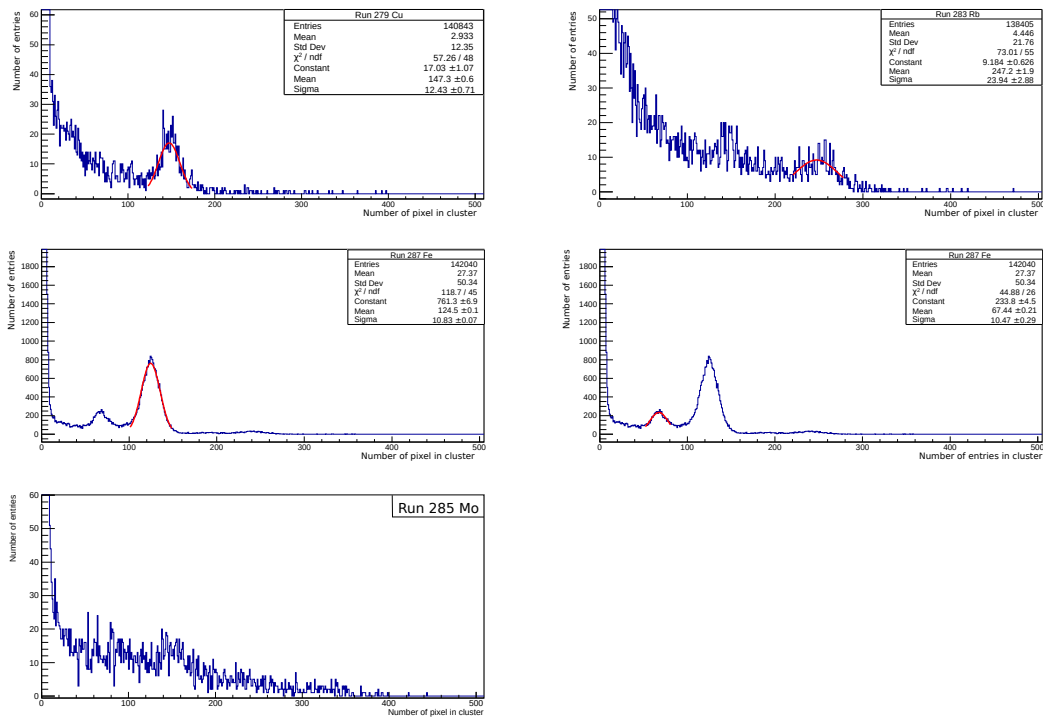


Fig. 5.13: Spectra for different sources and Gaussian fit.

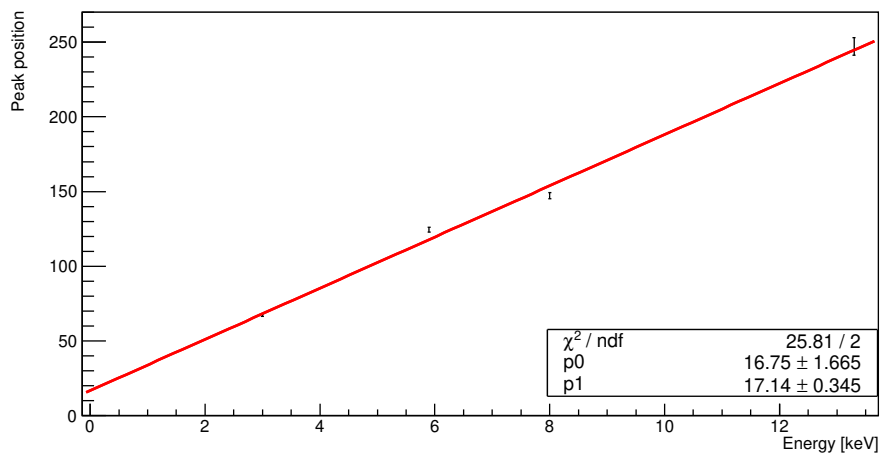
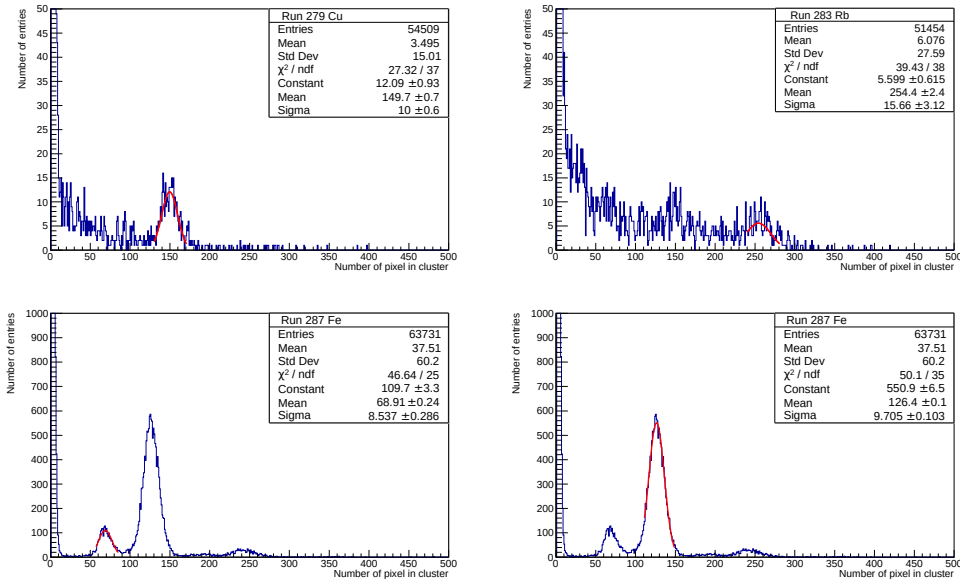


Fig. 5.14: Photon energy and peak position of the fitted Gaussian for the analysis with 25 clock cycles required for accepted pixel and no further cuts.

### 5.3.2 Modified cuts: Border cut

Using the same data sets, the analysis is run again with a cut to remove cluster with a center closer than a chosen value to the chip border. The goal is to remove partial or distorted cluster. To exclude the 25 outermost pixel when the cluster radius is set to 25, the required distance is 50 pixel. The resulting energy calibration is shown in figure 5.16.



**Fig. 5.15:** Spectra for different sources and Gaussian fit. Pixel require 25 clock cycles to be accepted, cluster center more than 50 pixel distance from chip border.

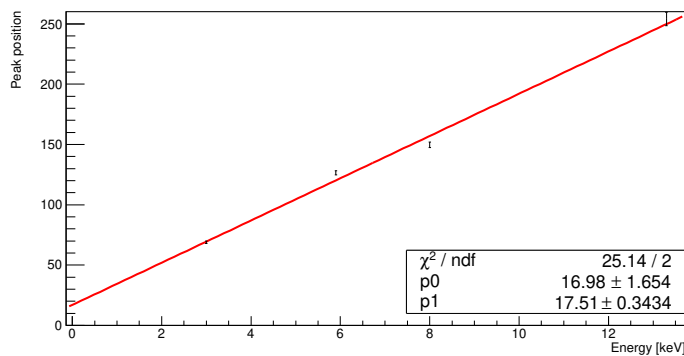


**Fig. 5.16:** Photon energy and peak position of the fitted Gaussian for the analysis with 25 clock cycles required for accepted pixel and 50 pixel distance between center of cluster and chip border.

### 5.3.3 Modified cuts: Pixel threshold

The next change is a lowered threshold to accept a pixel as hit, set to 15 clock cycles instead of 25. The border cut is kept the same. The spectra are shown for the different runs, using these parameters for the algorithm, in figure 5.17.

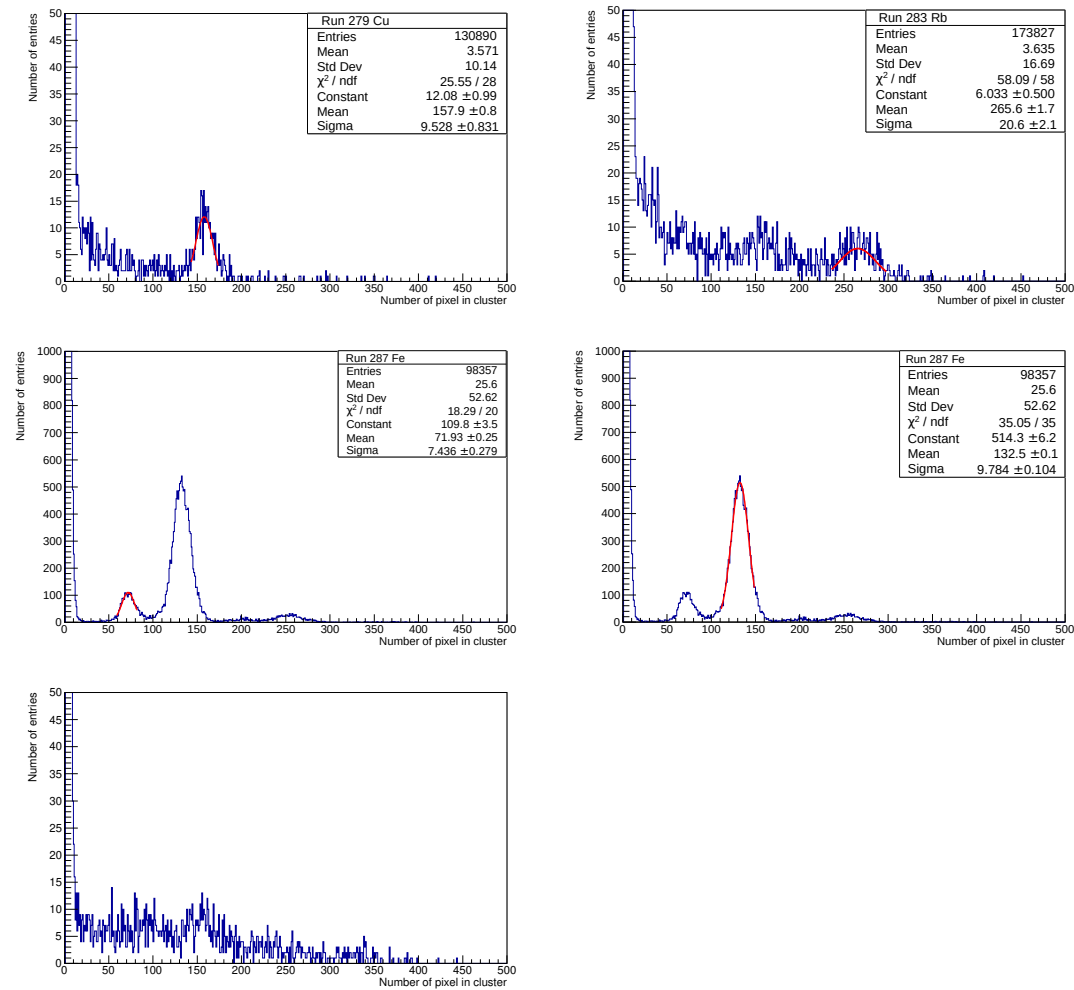


**Fig. 5.17:** Spectra for different sources and Gaussian fit. Pixel require 15 clock cycles to be accepted, cluster center more than 50 pixel distance from chip border.

It is visible that a reduction in the number of entries happens. Since the cut on the border reduces the effective area for the detection, is expected. The increased number of proto clusters during the reconstruction increases the run time significantly, since the number of distances calculated increases as  $N^2$  and the number of proto cluster merger as  $N$ . All changes to fit parameters are less than 10%. The linear fit for the energy is shown in figure 5.18.

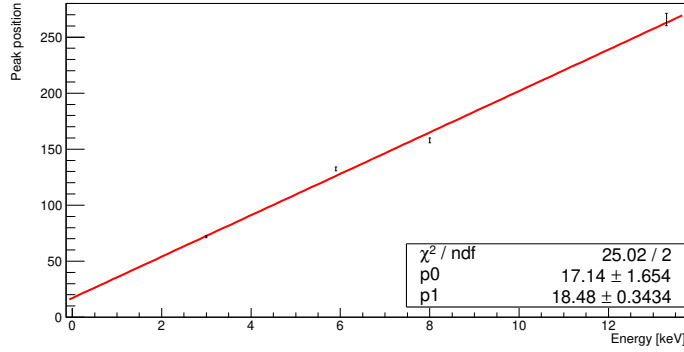


**Fig. 5.18:** Photon energy and peak position of the fitted Gaussian for the analysis with 15 clock cycles required for accepted pixel and 50 pixel distance between center of cluster and chip border.

### 5.3.4 Summary of cuts

It should be noted that during all analysis, the number of hits in a cluster is less than the average number of electrons produced. This can be used to estimate the efficiency for electron detection. For example for iron, 133 hits are recorded, while 215 electrons are produced on average. This yields a detection probability of approximately 60 %. For the other sources, the detection probability is 54 % for rubidium and copper. For the 3 keV escape peak the efficiency increases even further to 65 %.

Source	Fe	Cu	Rb
Energy[keV]	5.9	8	13.4
Efficiency	0.60	0.54	0.54

**Tab. 5.3:** Detection efficiency for the different X-ray energies.

In table 5.4 the effects of the different cuts on the peak position are shown. The cut to borders, rejecting distorted clusters, may have a small effect of shifting the peak to higher values. This effect is much less than the effect of lowering the threshold at which a pixel is accepted by the algorithm. Lowering this cut increases the peak position. This is also visible in the energy calibration, with agreement within one standard deviation for the results for the 25 clock cycle cut, but more than two standard deviations disagreement for the slope between the cut at 25 and 15 clock cycles. The difference between the cut at 15 and 25 clock cycles is less than 7 %.

Source	Energy [keV]	TOT 25	Border 50, TOT 25	Border 50, TOT 15
Cu	8	147.3 ± 0.6	149.7 ± 0.7	157.9 ± 0.8
Rb	13.4	247.2 ± 1.9	254 ± 2	265.6 ± 1.7
Fe	5.9	124.5 ± 0.1	126.4 ± 0.1	132.5 ± 0.1
Fe	3.0	67.4 ± 0.2	68.9 ± 0.2	71.9 ± 0.3
Slope		17.1 ± 0.3	17.5 ± 0.3	18.5 ± 0.3
Offset		16.8 ± 1.6	17.0 ± 1.6	17.1 ± 1.6

**Tab. 5.4:** Comparison of peak positions between different cuts and the resulting energy calibration.

Another interesting property is the root mean square (RMS) of the peaks. This is shown as a summary in table 5.5. The broader peaks at higher energy are most likely caused by several effects. The first effect may be reduced statistics and a decreased signal to noise ratio. The second effect is the increased contribution of the  $K_\beta$  line, increasing the width of the observed peaks. Especially the introduction of the border cut removes partial and distorted cluster, leading to a shift to higher mean values and narrower peaks.

Source	Energy [keV]	TOT 25	Border 50, TOT 25	Border 50, TOT 15
Cu	8	12.4 ± 0.7	10.0 ± 0.6	9.5 ± 0.8
Rb	13.4	24 ± 3	16 ± 3	20 ± 2
Fe	5.9	10.83 ± 0.07	9.7 ± 0.1	9.8 ± 0.1
Fe	3.0	10.5 ± 0.3	8.5 ± 0.3	7.4 ± 0.3

**Tab. 5.5:** Comparison of the peak RMS between different cuts.

The  $K_\beta$  lines could not be resolved at the current energy resolution and statistics.

## 5.4 Additional analysis

Because of the high statistics, some additional tests are done with the data of run 287. The applied cuts are a cut at 15 clock cycles and a distance to the border of 50 pixel. For fitting of a Gaussian, a cluster has to contain at least 50 pixel and a distance of 50 pixel or more to the border. The cut on the number of pixel contained to be accepted is chosen at the low edge of the escape peak. The starting parameters for the minimization of equation 4.2 using the Minuit package of root are chosen as the center and RMS of the cluster. The histogram for fitting contains only the pixel assigned to the cluster. A correlation plot between the sum the TOT of all pixels assigned to a cluster and the number of pixels in the cluster, is

shown in figure 5.19. It was created from results of the cluster algorithm before fitting and shows several features. Around 0, there are many entries that are random noise. There is a linear behaviour between the number of pixels in a cluster and the TOT collected in the cluster. This is to be expected, as the average TOT caused by a single electron should be homogeneous across the chip. There is also an increase in entries for around 125 pixel, corresponding to the entries for building up the full absorption peak. A few entries seems to deviate from the linear behaviour, showing more clock cycles for the number of pixel.

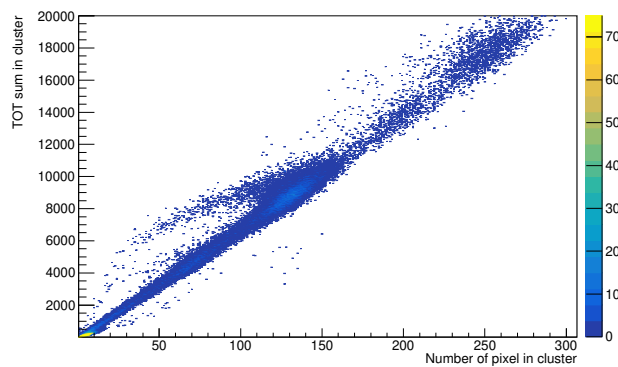


**Fig. 5.19:** Total TOT in a cluster vs number of pixels for run 287.

Another interesting plot is the distribution of TOT values of pixels assigned to clusters. This distribution is shown in figure 5.20 and only contains pixel that are assigned to cluster with more than 15 entries. The sharp cut off at 15 clock cycles is an artifact, since pixel have to exceed 15 clock cycles to be accepted by the clustering algorithm as hit. This distribution may be compared to the second plot in the figure, containing all pixel. The interesting region is shown for comparison in figure 5.20. The suppression in lower clock cycles has several reasons. The hard cut at 15 clock cycles for the algorithm is visible in the TOT distribution of the pixel assigned to clusters. There is some further reduction in the area of low clock cycles. This may be because chip noise may appear anywhere on the chip and has low TOT values, while hits by electrons on the InGrid chip appear most of the time as part of the cluster. This is also evident by the very similar shape of both distributions in the area of higher TOT values. The absolute entry numbers are different, because some cluster are rejected by the border cut.

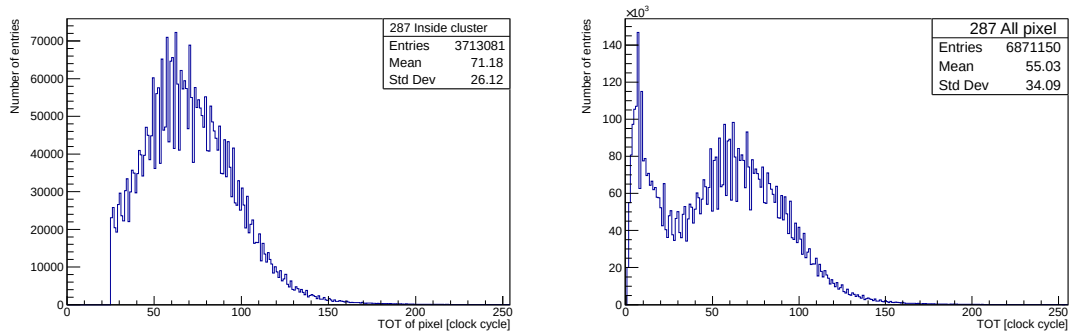


**Fig. 5.20:** TOT of pixel in an accepted cluster on the left side and for comparison TOT of all pixels on the right side.

An interesting parameter may be the TOT value of the central pixels in a cluster, since the likelihood of several electrons in the same hole of the InGrid is higher in the central region. A histogram containing only the central 3x3 area of the cluster is shown in figure 5.21. It has to be noted that this collects all pixel in the area, including pixel that have been rejected by the clustering algorithm. No structures in the distribution show multiple electrons in the same grid hole. It is possible that the width of the peaks for multiple electrons are too broad to be easily visible. To test for this, the average TOT of the pixel per hit is calculated and shown in the same figure. It should be noted that the statistical errors on the map are large, because of low statistics, with an average of 125 hits. A possible solution to this, which would reduce or even remove this problem, is a equalisation with each pixels average TOT before the analysis. This may become the topic of further analysis.

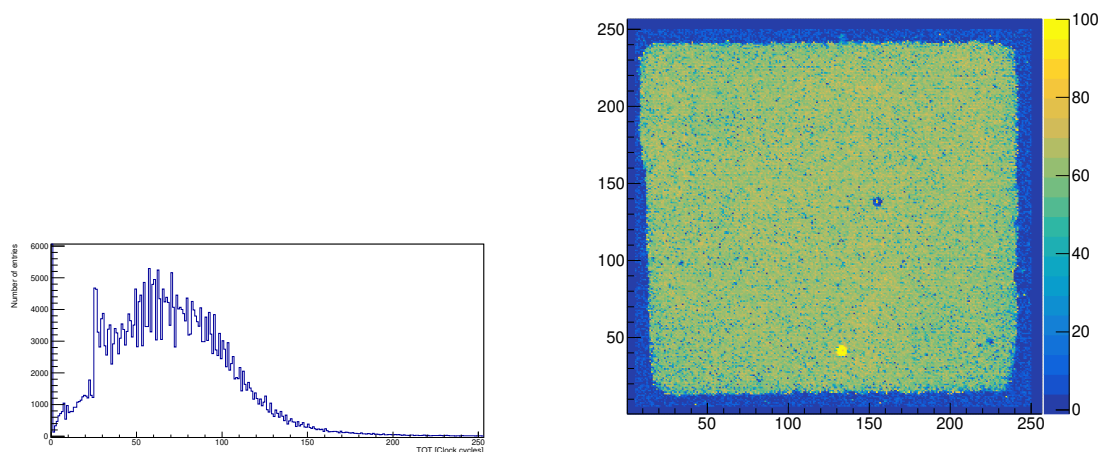


**Fig. 5.21:** Distribution of the TOT of the cluster for the central 9x9 pixel and map of the average TOT.

A comparison between the peak position calculated by the fit and the direct calculation without fit is shown in figure 5.22. It is visible that the deviation between the two methods is very small. The cluster accepted for fitting are all within the central region and appear to have a homogeneous distribution.

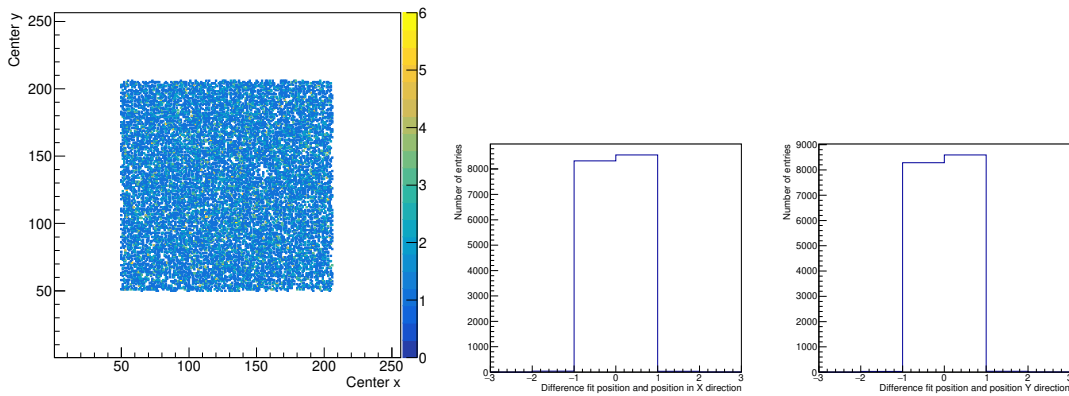


**Fig. 5.22:** Distribution of the center of the fit and deviation from the direct calculation.

Several ways to find the width of the cluster can be compared. The first and most simple method calculates the RMS of the pixel assigned while not taking the different TOT value into account. This method results in the distributions shown in figure 5.23, showing the correlation between the RMS in x and y direction, as well as the projections. The peak of the distribution is between 7 and 8, compared to the expected width of a cluster of approximately 7 pixel. Both values are in agreement. The RMS also shows a very strong correlation between the RMS in x and y direction, most likely caused by almost circular cluster shapes. The cluster with smaller RMS are most likely generated by photons absorbed closer to the chip. The shorter drift distance reduces the spread by diffusion. The RMS calculations show a regular structure with preferred values every 0.5 pixel. This is most likely an effect of the RMS being calculated with only integer values, since the pixel position is integer, as well as the information if it exceeded the threshold. The projections are smoothed using the 353QH smoothing algorithm included in root to remove these artifacts of binning.



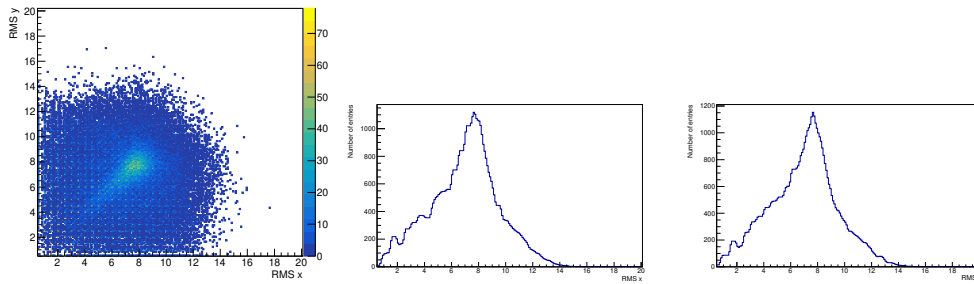


**Fig. 5.23:** Distribution of the RMS for the cluster and projections.

The next step compares the RMS of the fit before calculating the principal axis. Since the RMS for a Gaussian is  $\sigma$ , both values should be similar. The hard cut at 25 pixel radius by the clustering would cut the tails of the Gaussian above  $3\sigma$  and should not cause much difference. The plots are shown in figure 5.24. Both with and without fit show very similar results. One visible difference is the lack of the regular structure seen in the direct calculation from the pixel position, further suggesting that the regular structures in figure 5.23 are artifacts.

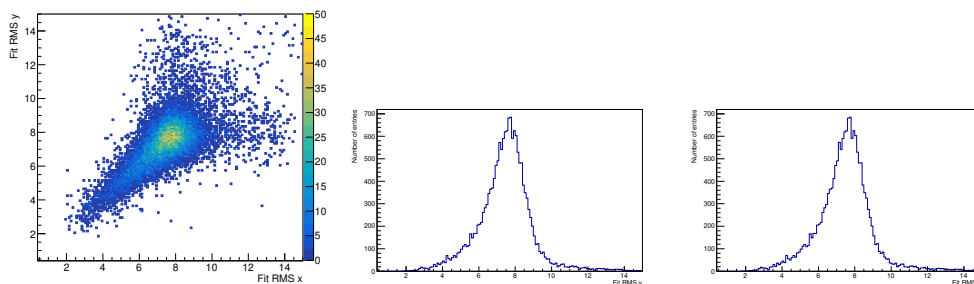


**Fig. 5.24:** Distribution of the RMS for the cluster and projections, extracted from Gaussian fit.

A direct comparison between the RMS calculated by both methods is shown in figure 5.25. Both values are very strongly correlated, with only few entries deviating from this behaviour. This is indicative that the fit to the clusters worked in most cases and a Gaussian describes the distribution of hits inside a cluster well.

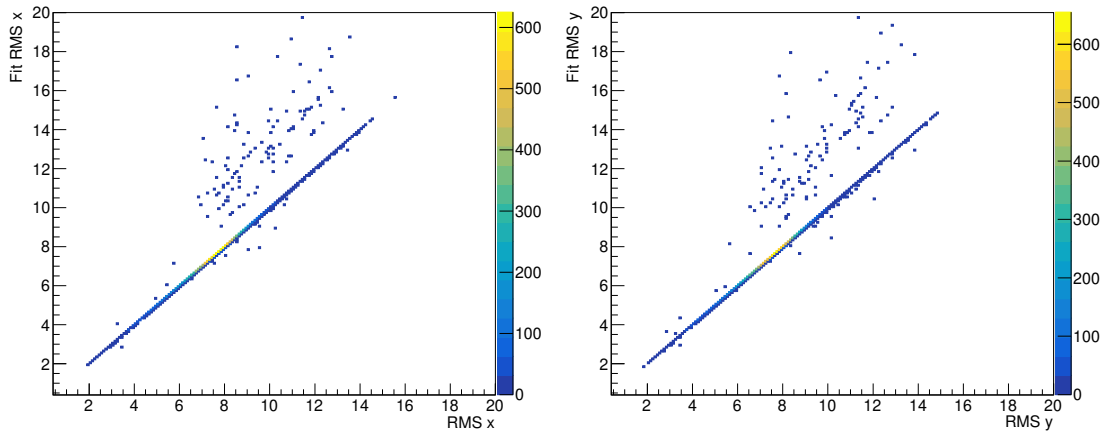


**Fig. 5.25:** Distribution of the RMS for the cluster, extracted from Gaussian fit compared to direct calculation.

The next step is the conversion from x and y coordinates to the principal axis of the cluster. The angle between the principal axis and the coordinate system of the chip is shown in figure 5.26. It should be noted that the angle is set to close to zero before the fit and a circular cluster has no well defined angle. This can also be explained in terms of corellations, since a circular cluster can be generated by multiplication of two Gaussians with the same width. These would have no corellations, thus giving an angle of zero. For symmetry reasons, the possible values for the angle cover an intervall of 90 degrees. Taking into account the results for the RMS, both with and without fit, the preference of zero in the distribution is caused by circular clusters.

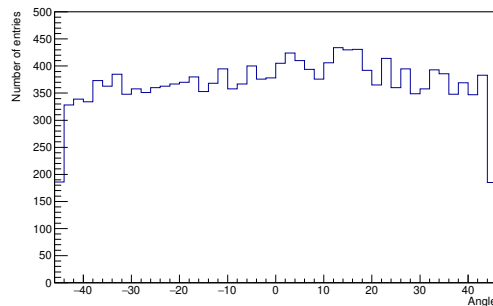


**Fig. 5.26:** Distribution of the angle of the cluster, extracted from Gaussian fit, in degree.

The resulting ditributions for the principal axis are shown in figure 5.27. It should be noted that the very circular cluster make this fit less reliable, since the corellation is small. The

range is in the interval  $(-45, +45)$  degrees

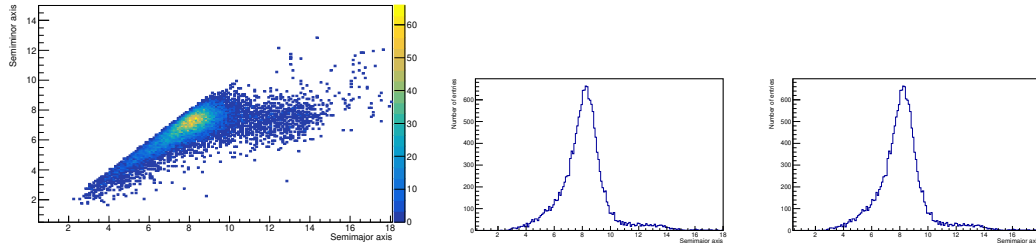


**Fig. 5.27:** Distribution of the principal axis for the cluster and projections, extracted from Gaussian fit.

For the ellipse, the eccentricity is shown in figure 5.28. The average value corresponds to a ratio between the principal axis of 0.85.

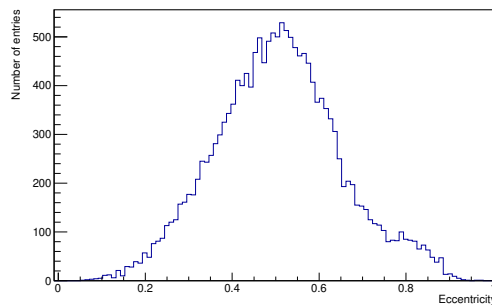


**Fig. 5.28:** Distribution of the eccentricity.

#### 5.4.1 Comparison of cluster parameters for different energies

A comparison of the RMS for different photon energies is done using the RMS from the fit. The difference between the direct calculation and the Gaussian fit is very small, as shown before, so the results can be applied in both cases. The RMS distributions for the remaining energies are shown in the figures 5.29 and 5.30. There is no difference between the different energies in terms of the peak position.

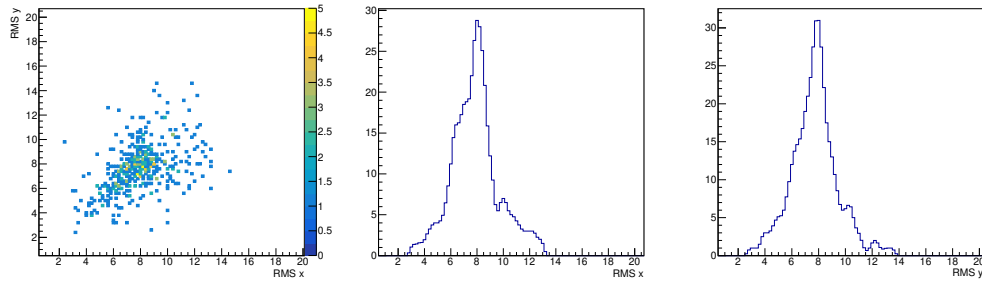


Fig. 5.29: Distribution of the RMS for the cluster and projections for copper.

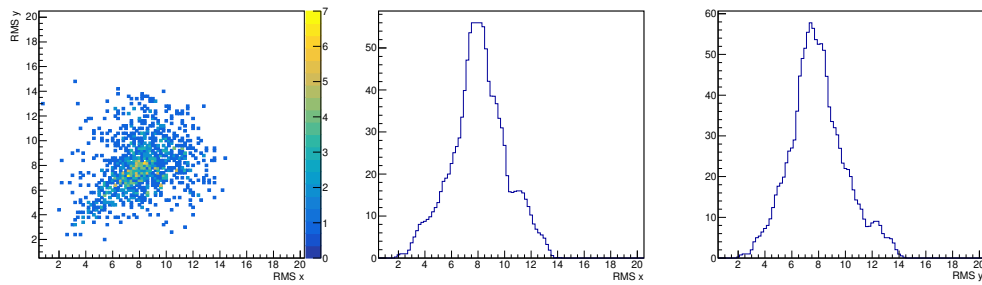


Fig. 5.30: Distribution of the RMS for the cluster and projections for rubidium.

## Conclusion

The detector and read out are working like designed. Gas leaks are small and and gas amplification is stable. Operation parameters for stable operation and little distortion during drift are found and the removal of hot pixels of the chip is efficient.

The reconstruction using the Cambridge-Aachen algorithm creates a spectrum for different sources and if multiple photons are in the same frame. After 410 V a further increase in amplification voltage showed no further increase in the peak positions of the spectrum. The dependency between the number of pixel and the photon energy showed a linear behaviour in the tested range, although more calibration energies may be useful to better characterise the linearity. The effect of different cuts was investigated. A cut on the cluster position, removing cluster close to the chip border, reduced the variation of the number of hits in the cluster and increased the average number of hits per cluster. The reduction of the minimal TOT for a pixel to be accepted for clustering further increased the average number of hits per cluster. The efficiency for electrons is at 60 % for the iron source at 5.9 keV and seems to decrease with higher energies.

A separation between the  $K_\alpha$  and  $K_\beta$  line was not possible at the current energy resolution and statistics. The identification of multiple hits in a single pixel was also no yet possible. The analysis of the cluster shapes showed a strong preference of circular cluster, while the average width of the cluster is in good agreement with the width expected from diffusion. It is also visible from the data that a two dimensional gaussian fit to a cluster gives results in very good agreement with the direct calculation of the mean and RMS. Further fitting of an ellipse worked for X-ray photons. It may be a useful tool for discrimination against charged particles or photons parallel to the chip surface. The width of the cluster appears to be almost independent of the photon energy.

In conclusion, the new chamber with InGrid readout works and is able to measure photon energies in the region of interest for axion searches in helioscopes.



## Bibliography

- [Aad+12] Georges Aad et al. “Observation of a new particle in the search for the Standard Model Higgs boson with the ATLAS detector at the LHC”. In: *Phys. Lett. B* 716 (2012), pp. 1–29. DOI: 10.1016/j.physletb.2012.08.020. arXiv: 1207.7214 [hep-ex].
- [Ake+19] M. Aker et al. “Improved Upper Limit on the Neutrino Mass from a Direct Kinematic Method by KATRIN”. In: *Phys. Rev. Lett.* 123.22 (2019), p. 221802. DOI: 10.1103/PhysRevLett.123.221802. arXiv: 1909.06048 [hep-ex].
- [Amc] *Data sheet 11196*.
- [Arm+19] E. Armengaud et al. “Physics potential of the International Axion Observatory (IAXO)”. In: *JCAP* 06 (2019), p. 047. DOI: 10.1088/1475-7516/2019/06/047. arXiv: 1904.09155 [hep-ph].
- [AS11] Yasser Assran and Archana Sharma. “Transport Properties of operational gas mixtures used at LHC”. In: (2011). arXiv: 1110.6761 [physics.ins-det].
- [Ber+10] M.J. Berger et al. *NIST Standard Reference Database 8 (XGAM)*. 2010.
- [BS82] M.J. Berger and S.M. Seltzer. *Stopping powers and ranges of electrons and positrons*. U.S. DEPARTMENT OF COMMERCE, 1982.
- [Clo+73] D. A. Close et al. “Yield Ratios,  $\frac{K\alpha}{K\beta}$ ,  $\frac{L\alpha}{L\beta}$ ,  $\frac{L\alpha}{L\gamma}$ , and  $\frac{L\alpha}{L\text{II}}$ , for X Rays Produced by Protons of 1.0 to 3.7 MeV”. In: *Phys. Rev. A* (4 1973), pp. 1873–1879. DOI: 10.1103/PhysRevA.8.1873.
- [Col19] *BabyIAXO: the first stage of the International Axion Observatory (IAXO)*. 2019.
- [CSS08] Matteo Cacciari, Gavin P Salam, and Gregory Soyez. “The anti-ktjet clustering algorithm”. In: *Journal of High Energy Physics* 04 (2008), pp. 063–063. ISSN: 1029-8479. DOI: 10.1088/1126-6708/2008/04/063.

- [Cud07] Xavier Lopart Cudiè. “Design and characterization of 64K pixels chips working in single photon processing mode”. PhD thesis. Mid Sweden U., Sundsvall, 2007. ISBN: 978-91-85317-56-1.
- [Fra12] Martin Fransen. “Gridpix: TPC development on the right track. The development and characterisation of a TPC with a CMOS pixel chip read out”. PhD thesis. <https://hdl.handle.net/11245/1.377402>: Institute for High Energy Physics (IHEF), Sept. 2012. ISBN: 978-90-6464-581-5.
- [HAP66] A. Halprin, C. M. Andersen, and H. Primakoff. “Photonic Decay Rates and Nuclear-Coulomb-Field Coherent Production Processes”. In: *Phys. Rev.* 152 (4 1966), pp. 1295–1303. DOI: 10.1103/PhysRev.152.1295. URL: <https://link.aps.org/doi/10.1103/PhysRev.152.1295>.
- [Ira+13] Igor Irastorza et al. “The International Axion Observatory IAXO. Letter of Intent to the CERN SPS committee”. In: (2013).
- [Kri12] Christoph Krieger. “Construction and First Measurements of a GridPix-Based X-Ray Detector”. MA thesis. Universität Bonn, Feb. 2012.
- [Pec08] R. D. Peccei. “The Strong CP problem and axions”. In: *Lect. Notes Phys.* 741 (2008). [3(2006)], pp. 3–17. DOI: 10.1007/978-3-540-73518-2\_1. arXiv: hep-ph/0607268 [hep-ph].
- [PQ77] R. D. Peccei and Helen R. Quinn. “Constraints imposed by CP conservation in the presence of pseudoparticles”. In: *Physical review D* 16.6 (Sept. 1977), pp. 1791–1797.
- [Pur12] Andrew Purcell. “Go on a particle quest at the first CERN webfest. Le premier webfest du CERN se lance à la conquête des particules”. In: BUL-NA-2012-269. 35/2012 (2012), p. 10. URL: <https://cds.cern.ch/record/1473657>.
- [Rad+19] Fons Rademakers et al. *root-project/root: First release of the v6-16 series*. Version v6-16-00. Zenodo, Feb. 2019. DOI: 10.5281/zenodo.2557526. URL: <https://doi.org/10.5281/zenodo.2557526>.
- [Red13] Javier Redondo. “Solar axion flux from the axion-electron coupling”. In: *JCAP* 1312 (2013), p. 008. DOI: 10.1088/1475-7516/2013/12/008. arXiv: 1310.0823 [hep-ph].
- [Shi18] Amir Noori Shirazi. “Track reconstruction for InGrid Chips for a Time Projection Chamber”. PhD thesis. Universität Siegen, 2018.
- [Tan+18] M. Tanabashi et al. “Review of Particle Physics”. In: *Phys. Rev. D* 98 (3 2018), p. 030001. DOI: 10.1103/PhysRevD.98.030001. URL: <https://link.aps.org/doi/10.1103/PhysRevD.98.030001>.



## Dank

Ich möchte insbesondere Professor Fleck dafür danken, das er diese Masterarbeit ermöglicht und unterstützt hat. Auch möchte ich Doktor Ulrich Werthenbach für die Unterstützung bei der Planung der neuen Kammer und die hilfreichen Gespräche danken. Desweiteren danke ich der mechanischen Werkstatt der Universität Siegen für die gute Zusammenarbeit beim Bau der Kammer. Bei meiner Familie und Freunden möchte ich für die Unterstützung und Ermutigung während des Studiums bedanken, insbesondere meinen Eltern. Zuletzt möchte ich den Mitgliedern der Experimentellen Teilchenphysik der Universität Siegen für die lehrreiche und interessante Zeit danken, sowie Carsten Schmidt und Yvonne Chim für das Korrekturlesen.



## Erklärung

Hiermit erkläre ich, dass ich die vorliegende Bachelor-Arbeit selbstständig verfasst und keine anderen als die angegebenen Quellen und Hilfsmittel benutzt, sowie Zitate und Ergebnisse Anderer kenntlich gemacht habe.

.....

(Ort)

(Datum)

.....

(Unterschrift)